THE ASTROPHYSICAL JOURNAL, 471:454–479, 1996 November 1

THE MASSES AND RADII OF THE ECLIPSING BINARY ζ AURIGAE[1]

PHILIP D. BENNETT[2] AND GRAHAM M. HARPER
JILA, University of Colorado and National Institute of Standards and Technology, Boulder, CO 80309-0440; pbennett@casa.colorado.edu, gmh@casa.colorado.edu

ALEXANDER BROWN
Center for Astrophysics and Space Astronomy, University of Colorado, Boulder, CO 80309-0389; ab@echidna.colorado.edu

AND

CHRISTIAN A. HUMMEL[3]
Universities Space Research Association, Washington, DC 20024; cah@fornax.usno.navy.mil
Received 1996 February 12; accepted 1996 May 29

ABSTRACT

We present a full determination of the fundamental stellar and orbital parameters of the eclipsing binary ζ Aurigae (K4 Ib + B5 V) using recent observations with the *Hubble Space Telescope* Goddard High Resolution Spectrograph (GHRS) and the Mark III long-baseline optical interferometer. The information obtained from spectroscopic and interferometric measurements is complementary, and the combination permits a complete determination of the stellar masses, the absolute semimajor axis of the orbit, and the distance. A complete solution requires that both components be visible spectroscopically, and this has always been difficult for the ζ Aur systems. The ζ Aur K star primary presents no difficulty, and accurate radial velocities are readily obtainable in the optical. However, the B star secondary is more problematic. Ground-based radial velocity measurements are hampered by the difficulty of working with the composite spectrum in the blue-violet region, the small number of suitable lines in the generally featureless optical spectrum of the B star, and the great width of the few available lines (the Balmer lines of hydrogen and a few weak He I lines) due to rapid rotation. We avoid the worst of these problems by using GHRS observations in the ultraviolet, where the K star flux is negligible and the intrinsic B star spectrum is more distinctive, and obtain the most accurate determination of the B star radial velocity amplitude to date. We also analyze published photometry of previous eclipses and near-eclipse phases of ζ Aur in order to obtain eclipse durations, which fix the length of the eclipse chord and therefore determine the orbit inclination. The long-baseline interferometry (LBI) yields, in conjunction with the spectroscopic solution, the distance to the system and thus the absolute stellar radius of the resolved K supergiant primary star, ζ Aur A. The secondary is not resolved by LBI, but its angular (and absolute) radius is found by fitting the model stellar flux plus an interstellar extinction model to the flux-calibrated GHRS data. We find $M_K = 5.8 \pm 0.2\ M_\odot$, $M_B = 4.8 \pm 0.2\ M_\odot$, $R_K = 148 \pm 3\ R_\odot$, and $R_B = 4.5 \pm 0.3\ R_\odot$ for the masses and radii of the ζ Aur stars. We determine the distance to ζ Aur to be 261 ± 3 pc.

Additionally, we refine the stellar parameters of the B star secondary presented in the 1995 spectroscopic study of Bennett, Brown, & Linsky. We also determine the effective temperature of the K star primary using values of the bolometric flux, angular diameter, and interstellar extinction derived in this study. The positions of the ζ Aur stars on the theoretical H-R diagram are compared to current evolutionary model tracks, and the resulting good agreement provides a strong check of the internal self-consistency of this analysis and the accuracy of the theoretical models. The ζ Aurigae stars are confirmed to be coeval with an age of 80 ± 15 Myr.

Subject headings: stars: binaries: eclipsing — stars: fundamental parameters — stars: individual (ζ Aurigae) — techniques: interferometric — techniques: radial velocities — ultraviolet: stars

1. INTRODUCTION

The ζ Aurigae stars have been extensively studied for more than 70 years, since these binary systems present the rare opportunity for spectroscopic observations along a known line of sight through the outer atmosphere of the evolved primary star. Observations are especially useful in the ultraviolet, where the flux from the primary is negligible and the secondary serves as a nearly ideal "light probe." We have observed the eponymous system, ζ Aur = HR 1612 = HD 32068 (K4 Ib + B5 V), at several epochs around the 1993 and 1995 eclipses with the Goddard High Resolution Spectrograph (GHRS) of the *Hubble Space Telescope* (*HST*) in a program primarily intended to study the extended atmosphere of the K supergiant star. The orbit of ζ Aur, with the GHRS observation epochs marked, is shown to scale in Figure 1.

Additionally, the ζ Aurigae systems are also of considerable interest because, as eclipsing double-lined binaries, they provide the best opportunity for determining accurate masses and radii of evolved late-type stars. The GHRS observations of ζ Aur prove to be extremely useful in improving the poorly known value of the radial velocity

[1] Based on observations made with the NASA/ESA *Hubble Space Telescope*, obtained at the Space Telescope Science Institute, which is operated by the Association of Universities for Research in Astronomy, Inc., under NASA contract NAS 5-26555.

[2] Present address: Center for Astrophysics and Space Astronomy, Campus Box 389, University of Colorado, Boulder, CO 80309-0389.

[3] Postal address: US Naval Observatory–AD5, 3450 Massachusetts Avenue NW, Washington, DC 20392-5420.

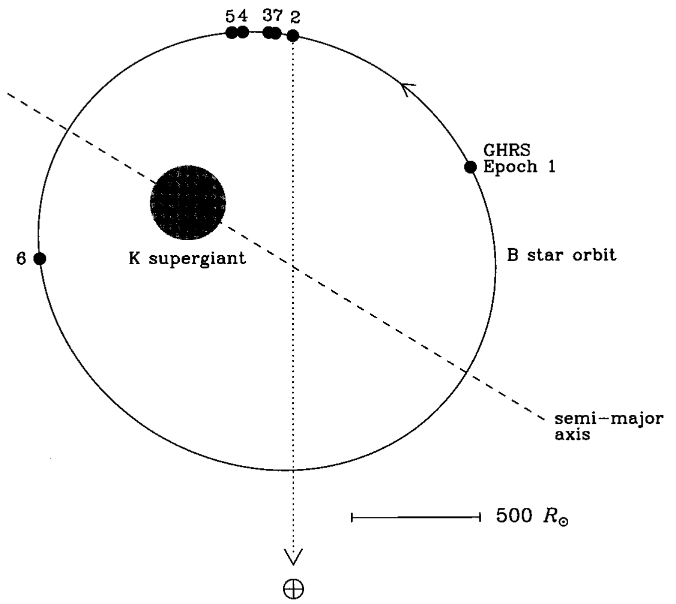

FIG. 1.—Orbit of ζ Aurigae drawn to scale. The positions of the secondary at the GHRS observation epochs are indicated, and the semimajor axis and the direction of the line of sight from Earth are also shown. The size of the K supergiant primary is shown to scale, but the actual size of the B star secondary is smaller than indicated in this diagram.

semiamplitude K_2 of the B star secondary, which immediately provides a more accurate estimate of the mass ratio M_B/M_K. From this beginning, we used recent interferometry (LBI) from the Mark III optical long-baseline interferometer[4] and a compilation of published eclipse photometry to undertake a complete reanalysis of the ζ Aurigae system. The resulting data set is sufficiently extensive to permit a complete solution of the system and, in many cases, to obtain independent evaluations of physical parameters (such as the B star gravity, both by spectroscopic methods and by direct evaluation from the stellar mass and radius). This redundancy provides extremely useful checks on the self-consistency of the solution. The result of this analysis yields accurate values of the masses and radii of both stars, the semimajor axis and orbit inclination, the distance to the system, and the interstellar extinction along the line of sight.

The organization of this paper is summarized as follows. In § 2, the radial velocity amplitude of the B star secondary, and the mass ratio of the stars, are found. In § 3, the Mark

[4] The Mark III long-baseline optical interferometer, located on Mount Wilson near Los Angeles, CA, is operated by the Remote Sensing Division of the Naval Research Laboratory (NRL) with funding from the Office of Naval Research.

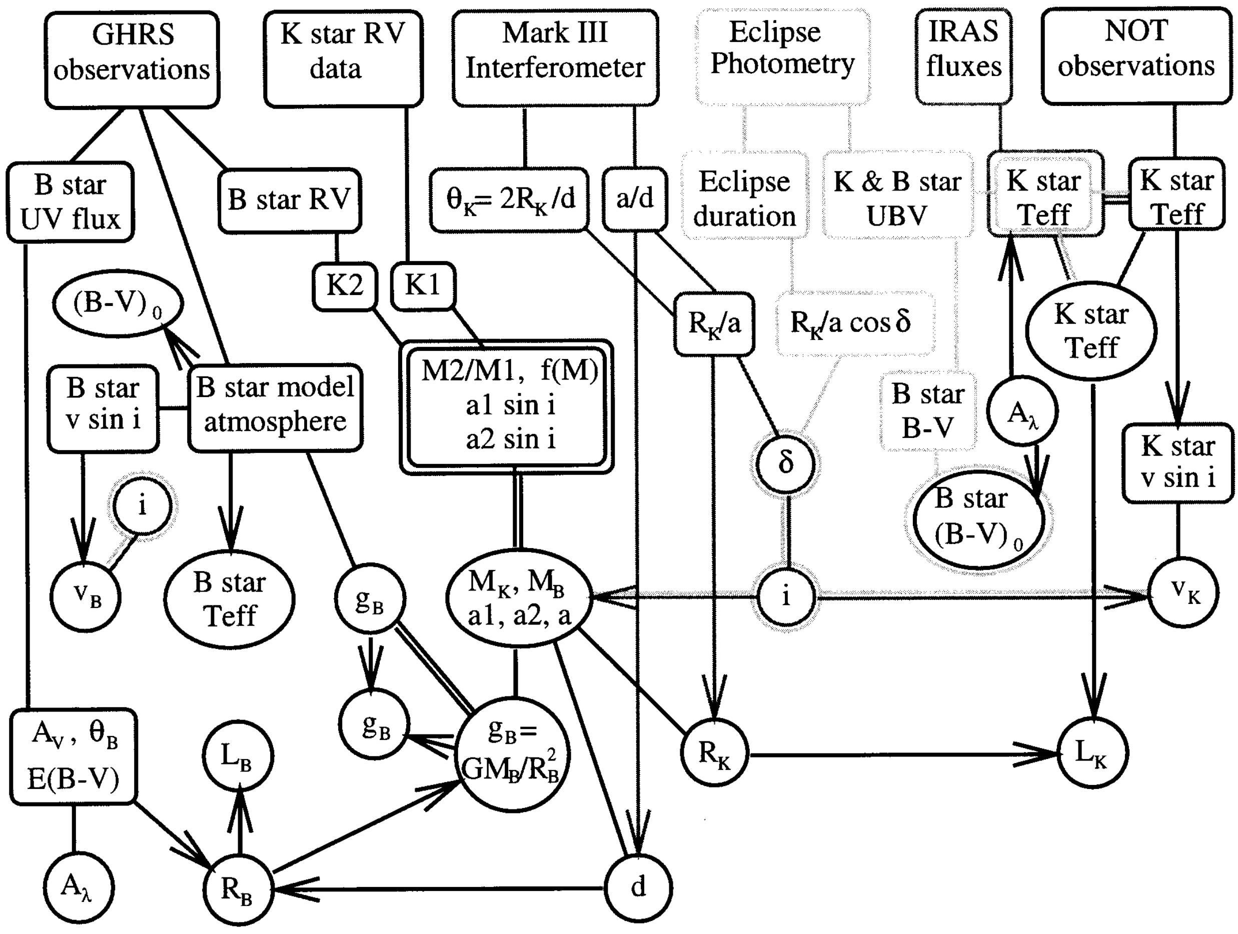

FIG. 2.—Schematic diagram showing an overview of the observational data and the analysis procedures used in this study. The logical flow proceeds from top to bottom and from left to right unless otherwise indicated by an arrow. Observations and intermediate results are denoted by a rectangular box, while fundamental, derived quantities appear in circles. The different shades of gray reflect the different types of observations. Double lines connecting the same quantity derived independently indicate a consistency check. The notation is consistent with usage in the text: *M*, *L*, *R* refer to stellar masses, luminosities, and radii, respectively; *g* refers to the stellar gravity; θ refers to the stellar angular diameter; *a* refers to the semimajor axis of the orbit; *i* refers to the orbital inclination; δ refers to the eclipse latitude; and *d* is the distance to the system. The stellar rotational velocity is denoted by *v*, and *f*(M) is the mass function of the binary system. Finally, A_V and A_λ refer to the interstellar extinction at *V* magnitude and at wavelength λ, respectively.

III long-baseline interferometry is used, along with published eclipse photometry, to determine the stellar masses, the absolute radius of the K star primary, and the distance to the system. In § 4, the absolute radius of the B star secondary, and the interstellar extinction along the line of sight, are determined consistently with the flux-calibrated GHRS observations. In § 5, the luminosities of both ζ Aur stars are calculated, and the stars and their respective model evolutionary tracks and isochrones are placed on the theoretical H-R diagram, from which the age of the system is found. Finally, in § 6, we present a summary of the results and checks of self-consistency and briefly discuss areas in which further substantial improvements in the accuracy of the fundamental parameters are feasible.

This study derives fundamental stellar and orbital parameters of the ζ Aurigae binary system using a variety of observational constraints. We present in Figure 2 a flowchart showing an overview of the observations and the analysis procedures. This diagram clearly indicates the independent and complementary nature of the spectroscopic and interferometric analyses that proved essential to determining accurately and unambiguously the stellar and orbital parameters of this important binary system.

2. RADIAL VELOCITY CURVE OF THE B-TYPE SECONDARY

2.1. *Historical Summary*

Obtaining the radial velocity of the primary spectrum is straightforward. Harper's (1924) observations at Victoria, combined with some later observations at Mount Wilson and Lick, still comprise the most extensive published set of radial velocity data for the K star primary, ζ Aur A. Wood's (1951) value of the period, 972.162 days, and Wright's (1970) determination of the orbital elements have stood almost unchanged to this day.

In the secondary spectrum, the Balmer lines are the only suitable lines for radial velocity determinations in the optical. Since these occur where the spectrum is composite, radial velocity determination of the secondary requires reconstruction of the pure B star spectrum. This, in principle, can be achieved by subtraction of the pure K star spectrum obtained during total eclipse from the composite spectrum. However, this subtraction requires a knowledge of the relative fluxes of the two stars. Since this information is not generally available from ground-based coudé spectrographs, the flux ratios must instead be inferred from the composite spectrum. In the older photographic work the low signal-to-noise ratio (S/N) of photographic spectra and the nonlinear response of photographic emulsions made the subtraction of spectra a difficult task. Lee & Wright (1960) used this method of subtraction spectrophotometry to determine the semiamplitude, K_2, of ζ Aur B. Their original analysis yielded discrepant values of 34.9 km s^{-1} and 21.4 km s^{-1} for two epochs and an indeterminate value for a third epoch. This method was more successfully applied by Wright (1970) to a larger data set, combining Lee & Wright's (1960) ζ Aur data with additional Victoria observations, to obtain $K_2 = 31.4 \pm 2.8$ km s^{-1} for the secondary spectrum.

Popper (1961) obtained the value $K_2 = 34 \pm 3$ km s^{-1} for ζ Aur by measuring the positions of selected Balmer lines in the B star relative to standard lines in the K star spectrum. This procedure yields the value $K_1 + K_2$ from which K_2 is found by subtracting the relatively well-determined value of K_1. Koppmann (1985) also analyzed photographic spectra of ζ Aur using Popper's (1961) method to obtain $K_2 = 30.6 \pm 6.0$ km s^{-1}. The limitations of trying to extract reliable radial velocities of the ζ Aurigae secondaries from composite spectra recorded on photographic emulsions are seen by examination of Koppmann's radial velocities. The scatter in the derived velocities is so large that these data would be consistent with *no* velocity variation without the extra constraint provided by the known shape of the velocity curve.

Griffin et al. (1990) used a cross-correlation technique to measure the radial velocity shift between two spectra of ζ Aur B at orbital phases 0.23 and 0.54. Although Griffin et al. (1990) do not quote a value for K_2, they derive a mass ratio of $M_K/M_B = K_2/K_1 = 1.3$ and masses of $M_K = 7.0\ M_\odot$ and $M_B = 5.4\ M_\odot$. The cross-correlation method employed by Griffin et al. (1990) is probably the most accurate of the methods used to estimate K_2, and the method adopted for our determination of the B star radial velocity amplitude is based on this approach. R. F. Griffin has been observing ζ Aurigae for nearly 15 years with both the original Cambridge spectrometer and Coravel at Haute-Provence and has kindly provided the authors with a revised orbit based on this extensive data set. The Griffin (1995) velocity semiamplitude is $K_1 = 23.35 \pm 0.14$ km s^{-1}. The velocity amplitudes and stellar masses found from the various spectroscopic investigations are summarized in Table 1. The orbital elements derived from the Griffin data set are given in Table 2.

2.2. *Determination of the Radial Velocity from GHRS Observations*

We observed ζ Aur with the GHRS at seven epochs around the 1993 April and 1995 December eclipses. The K star flux is negligible in this region of the ultraviolet, and so the problems of working with a composite spectrum are avoided. The spectrum of the B star shows substantial structure due to strong photospheric absorption features of Si II, C III, and H I Lyα. These considerations make observations of ζ Aur in the ultraviolet near 1200 Å well suited for determining the B star radial velocity. The phase coverage of our observations is nearly optimal for radial velocity

TABLE 1

RADIAL VELOCITY ANALYSES OF ζ AURIGAE

Source	K_1 (km s^{-1})	K_2 (km s^{-1})	M_1 ($M_\odot$)	M_2 ($M_\odot$)
Popper 1961	22.7 ± 0.3	34 ± 4	8.3 ± 1.5	5.6 ± 1.1
Wright 1970	24.6 ± 0.4	31.4 ± 2.8	7.6 ± 1.2	5.9 ± 1.5
Koppmann 1985	21.8 ± 1.3	30.6 ± 6.0	6.4 ± 1.7	4.5 ± 0.9
Griffin 1995	23.35 ± 0.14	...	...	...
Bennett et al. 1995	...	28.2 ± 0.6	5.8 ± 0.2	4.8 ± 0.2

TABLE 2

ζ Aurigae Orbital Elements

Element	Griffin 1995	Mark III
Period P (days)	972.183[a]	...
Eccentricity, e	0.400 ± 0.004	0.37 ± 0.02
Longitude of periastron, ω (deg)	328.5 ± 0.8	330 ± 3
Periastron passage, T	JD 2,441,373.6 $\pm$ 1.8	JD 2,447,212 $\pm$ 5
Mid-eclipse	JD 2,438,386.540[a]	...
Position angle of the ascending node, Ω (deg)	...	163.9 ± 1.0
Velocity semiamplitude:		
K_1 (km s^{-1})	23.35 ± 0.14	...
K_2 (km s^{-1})	28.2 ± 0.6[a]	...
Systemic velocity, V_0 km s^{-1}	$+12.21 \pm 0.07$	...
Semimajor axis, a (mas)	...	16.2 ± 0.1
Inclination, i (deg)	87.0 ± 1.3[a]	87.3 ± 1.0
K supergiant angular diameter (mas)	...	5.27 ± 0.10
Magnitude differences:		
Δm_{I_C}	...	3.76 ± 0.05
Δm_V	...	2.22 ± 0.05
Δm_B	...	0.9 ± 0.1

[a] This analysis.

determination since it includes times near the radial velocity extremes, as well as a sampling of intermediate velocities. The times, orbital phases, and true anomalies of these observation epochs are given in Table 3. The phase, by definition, is zero at primary mid-eclipse. For a description of the ζ Aurigae GHRS data set, see Brown et al. (1996).

All of the numerous, strong Si II features are resonance multiplets and are heavily contaminated with overlying wind and interstellar lines. Thus, the stellar line cores are not visible, and we must work solely with the line wings. The cleanest of the well-observed Si II features is the UV 4 multiplet at 1260–1265 Å, with strong lines at 1260.421 Å and 1264.737 Å, and a weaker line at 1265.001 Å blended with the latter. The peak between these lines, near 1263 Å, rises almost to the continuum. Since the entire region of this peak, 1261–1264 Å, is affected by the wings of either the Si II line at 1260.421 Å or the lines at 1264.737 and 1265.001 Å, we expect the shape of the spectrum to be especially sensitive to velocity shifts. The 1261–1264 Å region is free of obvious wind lines and was observed at epochs 1, 2, 3, and 6 with a wavelength calibration performed before each observation. For these reasons, we have used the 1260–1265 Å region for determining the radial velocities of the B star. All GHRS observations in this spectral region were made using the G160M grating with the small science aperture (SSA). The co-added, calibrated GHRS spectra in this spectral region obtained at epochs 1 and 2 is shown in Figure 3*a* and at epochs 3 and 6 in Figure 3*b*. In these figures, the portions of the spectra that have been assumed to be photospheric in origin are shown in black, while regions of overlying circumstellar and interstellar absorption are displayed in gray.

The procedure followed was to difference the B star spectrum for pairs of epochs and to infer the radial velocity shift between these observations, a technique that is more accurate than attempting to directly measure absolute velocities. The wind and interstellar absorption lines were removed, and the resulting pure B star spectra were Fourier smoothed to 7.3% of the Nyquist frequency, as described in Bennett, Brown, & Linsky (1995, hereafter Paper I). This smoothing procedure effectively reduces the number of independent pixels under the line profiles from about 90 in the original GHRS spectrum to seven in the smoothed spectrum but yields an increase in the effective S/N of about a factor of 4.

The flux-calibrated spectra observed at the different epochs showed small (typically about 3%) variations in absolute flux. It was found that the ratio of the fluxes from different observation epochs was well represented by a linear variation with wavelength, except in the immediate vicinity of the photospheric absorption lines. Here, the imperfect cancellation of spectral lines at different radial velocities results in P Cygni–like features in the ratioed spectrum. Applying a wavelength shift, which corresponds

TABLE 3

GHRS Observations of ζ Aurigae

Epoch	Date	UT	Julian Date	Orbital Phase[a]	True Anomaly[b] (deg)
1......	1992 Aug 31	23:40	2,448,866.49	0.7798	218.6
2......	1993 Feb 6	15:34	2,449,025.15	0.9430	269.3
3......	1993 Feb 20	08:03	2,449,038.84	0.9571	276.1
4......	1993 Mar 6	06:58	2,449,052.79	0.9714	283.8
5......	1993 Mar 11	23:08	2,449,058.46	0.9773	287.1
6......	1993 Aug 9	21:38	2,449,209.40	0.1325	52.2
7......	1995 Oct 16	12:56	2,450,007.04	0.9532	274.2

[a] Calculated using the ephemeris of eq. (15).

[b] Calculated from the phase using the orbital elements of Griffin 1995.

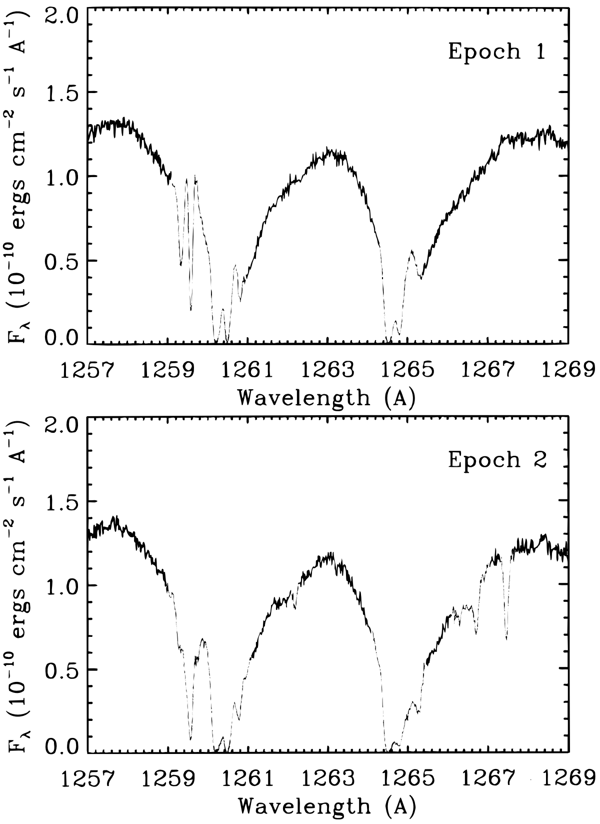

FIG. 3*a*

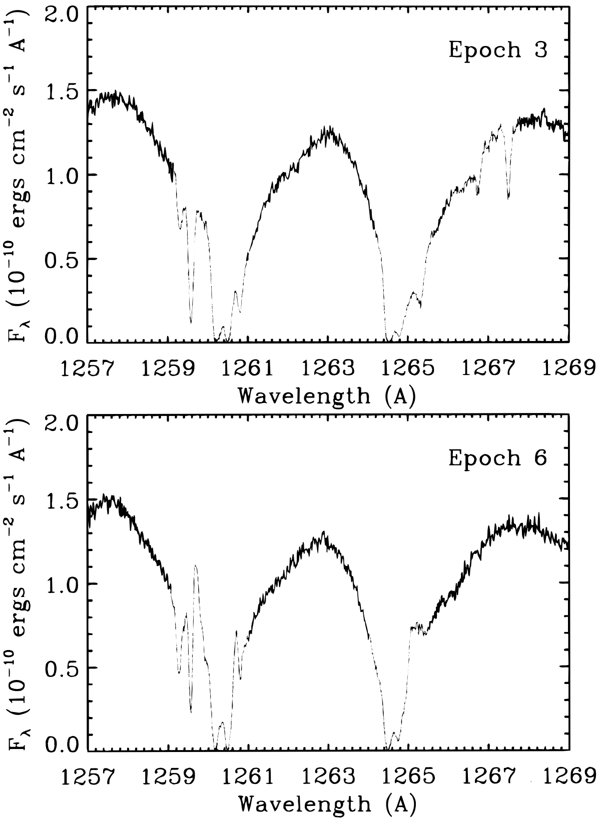

FIG. 3*b*

FIG. 3.—Co-added, calibrated, GHRS spectra of the region of the Si II UV 4 lines. The regions of the spectrum shown in light gray are where circumstellar and interstellar absorption obliterates the B star photospheric spectrum. (*a*) Spectra obtained at epochs 1 and 2. (*b*) Spectra obtained at epochs 3 and 6.

to the actual differential radial velocity shift of the B star between the observation times, to one of the spectra before ratioing would in principle result in perfect cancellation of the spectral lines in the ratioed spectrum. Therefore, from a plot of a series of flux-ratio spectra with varying differential radial velocity shifts, we obtain an estimate of the actual B star radial velocity difference between the observation epochs by seeking the velocity shift that minimizes the amplitude of the spectral features in the ratioed spectrum. In Figure 4*a*, we demonstrate the application of this method to the comparison of the spectra obtained at epochs 1 and 6. The flux ratio, F_λ^1/F_λ^6, is shown as a function of the applied radial velocity shift $\Delta V_{16}^{\mathrm{B}}$, where

$$\Delta V_{ij}^{\mathrm{B}} \equiv V_i^{\mathrm{B}} - V_j^{\mathrm{B}} . \tag{1}$$

The superscript indicates the velocities refer to the B star, while the subscripts denote the observation epochs. It is apparent from Figure 4*a* that $\Delta V_{16}^{\mathrm{B}} \approx +60\ \mathrm{km\ s^{-1}}$.

With the radial velocity shift given by $\Delta V_{ij}^{\mathrm{B}}$ applied, the ratio spectrum is well fit by a straight line. This linear fit yields the desired differential flux calibration between the two observations. It is important to note that this fit cannot be reliably done without first correcting for the radial velocity shift, since otherwise the ratioed spectral lines bias the resulting fit. We used this flux ratioing procedure to obtain all of the six possible differential flux calibrations between epochs 1, 2, 3, and 6. The analysis described in the rest of this section involves comparing relatively small differential changes in the B star spectrum observed at two different epochs in order to determine differential radial velocity shifts. In order to minimize errors due to variations in the absolute flux calibration between pairs of observations, the flux at the later observation was corrected by applying the differential flux correction found by the above procedure before any further analysis was done. This procedure ensured that the absolute flux calibration of the two spectra being compared was consistent. This differential calibration has been implicitly applied to all fluxes (denoted F_λ^i, where i is the observation epoch) subsequently referred to in this section.

To determine more accurately the differential radial velocity shifts between epochs, e.g., between epochs 1 and 6, we examined the behavior of the difference spectrum, $\Delta F_\lambda^{16}/F_{\max}^6$, as a function of the radial velocity shift $\Delta V_{16}^{\mathrm{B}}$ applied to the epoch 1 spectrum. Here $F_{\max}^6$ is the maximum flux value at epoch 6 over the region 1245–1285 Å and $\Delta F_\lambda^{16} = F_\lambda^1 - F_\lambda^6$. We show the behavior of the flux difference, $\Delta F_\lambda^{16}/F_{\max}^6$, as a function of the applied radial velocity shift in Figure 4*b*. In the absence of random and systematic errors, the difference spectrum will vanish when the applied radial velocity shift cancels the difference in orbital radial velocity between the observations. This technique reduces the determination of the radial velocity to the measurement of a null result. In practice, we compute the residual ε, or mean-square deviation from zero, of the difference spectrum and determine the velocity shift which minimizes the residual. More precisely, we define

$$\varepsilon = \sum_{\lambda=\lambda_1}^{\lambda_2} \frac{w_\lambda}{\sigma^2} \left(\frac{\Delta F_\lambda^{ij}}{F_{\max}^j}\right)^2 , \tag{2}$$

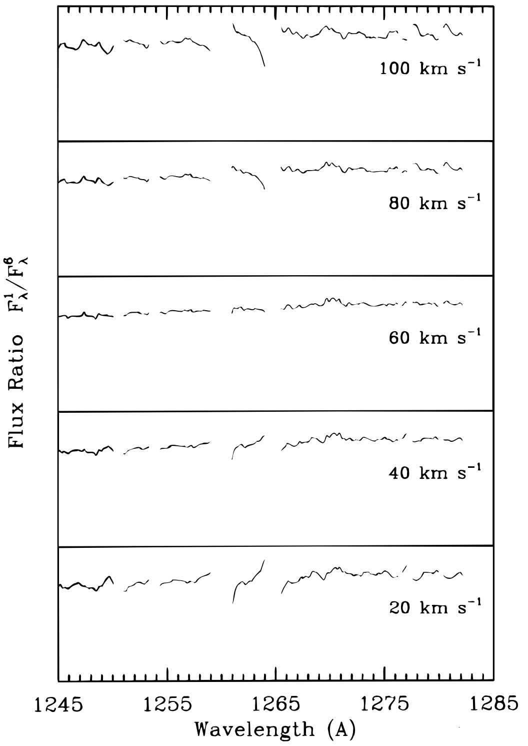

FIG. 4*a*

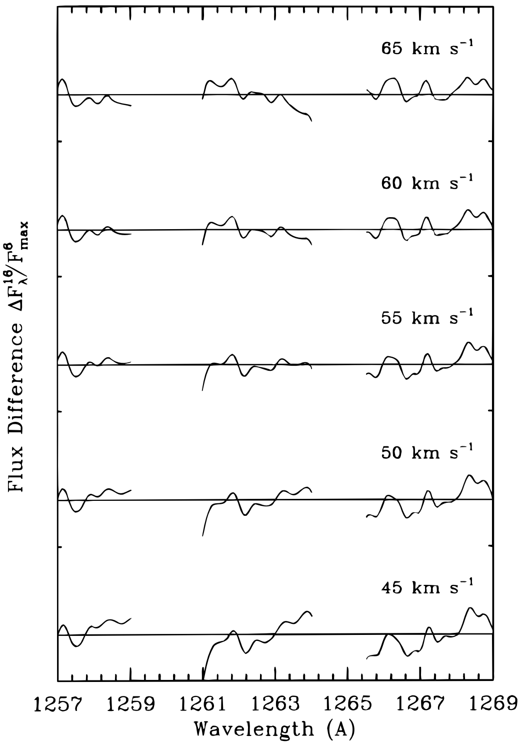

FIG. 4*b*

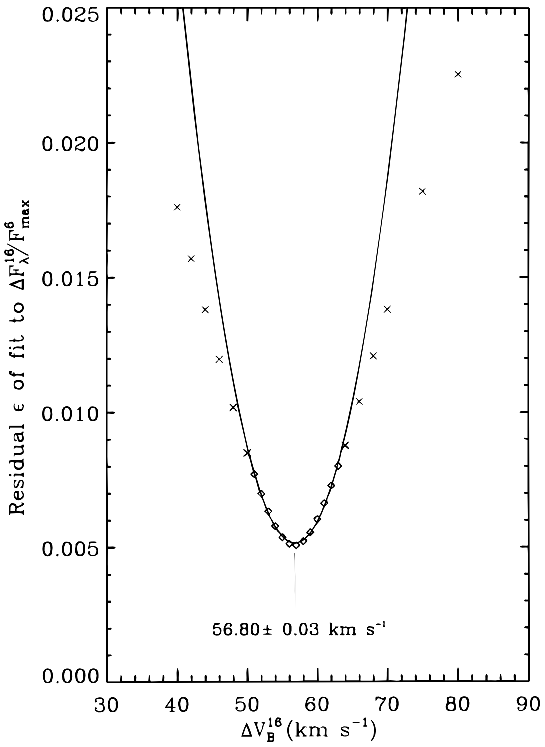

FIG. 4*c*

FIG. 4.—(*a*) Ratio of fluxes at epochs 1 and 6 as a function of radial velocity difference. The gaps in the spectra are the regions where the B star photospheric spectrum has been obliterated by circumstellar and interstellar absorption. The indicated radial velocity has been *subtracted* from the epoch 1 spectrum before the flux ratio F^1_λ/F^6_λ is evaluated. In the absence of random and systematic errors, a smooth curve is expected when the correct radial velocity shift is applied. In this case, the radial velocity difference between the spectra is about 60 km s^{-1}. (*b*) The difference of fluxes at epoch 1 and 6 (after the fluxes are normalized as described in the text) as a function of radial velocity difference. The gaps in the spectra are the regions where the B star photospheric spectrum has been obliterated by circumstellar and interstellar absorption. The indicated radial velocity has been *subtracted* from the epoch 1 spectrum before the flux difference is evaluated. In the absence of random and systematic errors, a null result is expected when the correct radial velocity shift is applied. (*c*) The residuals ε (rms deviations from zero) of the flux difference as a function of the applied radial velocity correction. We estimate the actual radial velocity difference between the GHRS observations at epochs 1 and 6 from the value of ΔV^{16}_B, where ε is minimum. The error appearing in this figure is the formal error of the location of the minimum as determined from the least-squares parabola fit. The actual uncertainty in the radial velocity is dominated by systematic effects and is very much larger than this value.

where the summation is over the pixels between wavelengths λ_1 and λ_2, σ is the standard error in the difference flux, and w_λ is an additional weight. The weight w_λ, normally unity, is set to zero in regions where the wind lines contaminate the photospheric spectrum to eliminate these wavelengths from the calculation of the residual. We illustrate the dependence of ε upon the applied velocity shift $\Delta V_{16}^{\mathrm{B}}$ in Figure 4*c*.

We obtained G160M grating spectra of the 1260–1265 Å region at epochs 1, 2, 3, and 6, and therefore, we proceed to determine the six radial velocity differences: $\Delta V_{16}^{\mathrm{B}}$, $\Delta V_{26}^{\mathrm{B}}$, $\Delta V_{12}^{\mathrm{B}}$, $\Delta V_{13}^{\mathrm{B}}$, $\Delta V_{23}^{\mathrm{B}}$, and $\Delta V_{36}^{\mathrm{B}}$. To examine the sensitivity of this procedure to the wavelength interval used, we determined all six $\Delta V_{ij}^{\mathrm{B}}$ values using three different spectral regions. First, we used the entire spectral region for case A: 1246–1281 Å. We would expect the sensitivity of the velocity determination to be poor in this case, since only portions of the spectrum near strong photospheric absorption lines are sensitive to changes in radial velocity. Second, we considered the region of the Si II line wings (the cores are lost due to overlying wind lines) for case B: 1257.5–1268 Å. Third, we restricted our interval to what we consider to be the cleanest and most sensitive region, case C: 1260–1264.5 Å, which includes the red wing of Si II 1260.421 Å and merges into the blue wing of Si II 1264.737 Å. The radial velocity differences found for cases A, B, and C are reported in Table 4.

We can estimate the numerical precision of these velocity determinations since the six $\Delta V_{ij}^{\mathrm{B}}$ variables are not independent. The four check sums C_{ijk}

$$C_{123} = \Delta V_{13}^{\mathrm{B}} - \Delta V_{12}^{\mathrm{B}} - \Delta V_{23}^{\mathrm{B}} = 0 \, , \tag{3}$$

$$C_{126} = \Delta V_{16}^{\mathrm{B}} - \Delta V_{12}^{\mathrm{B}} - \Delta V_{26}^{\mathrm{B}} = 0 \, , \tag{4}$$

$$C_{136} = \Delta V_{16}^{\mathrm{B}} - \Delta V_{13}^{\mathrm{B}} - \Delta V_{36}^{\mathrm{B}} = 0 \, , \tag{5}$$

$$C_{236} = \Delta V_{26}^{\mathrm{B}} - \Delta V_{23}^{\mathrm{B}} - \Delta V_{36}^{\mathrm{B}} = 0 \tag{6}$$

provide known values for comparison with numerical evaluations. Values of C_{ijk} calculated from the velocity differences should reflect the numerical dispersion about zero indicative of random errors in the $\Delta V_{ij}^{\mathrm{B}}$ determinations. We have calculated the mean C and standard deviation $\sigma(C)$ for each of the three determinations, and we list these values in Table 4. We also give an estimate of the standard deviation of the mean velocity difference

$$\sigma(\Delta V^{\mathrm{B}}) = \frac{1}{\sqrt{3}} \sigma(C) \, , \tag{7}$$

in Table 4. These statistics are limited since they involve averages of only four numbers (i.e., the four check sums), but they suggest that the random error in the relative velocities is considerably less than 1 km s^{-1}.

Examination of Table 4 verifies that case C has the smallest $\sigma(\Delta V^{\mathrm{B}}) = 0.21$ km s^{-1}. The mean $C = -0.07$ is statistically indistinguishable from zero, implying that the velocity determinations have not introduced a bias favoring certain observation epochs. A bias in the calculation of the $\Delta V_{ij}^{\mathrm{B}}$ values should yield a nonzero value of C since each C_{ijk} consists of the sum of one $\Delta V_{ij}^{\mathrm{B}}$ and the subtraction of two $\Delta V_{ij}^{\mathrm{B}}$ values. Systematic errors are more problematic in that they are not necessarily detected by the C_{ijk} check sums. For example, comparison of case B and case C shows that the value of $\Delta V_{26}^{\mathrm{B}}$ decreases by 3.6 km s^{-1} while $\Delta V_{12}^{\mathrm{B}}$ increases by 2.8 km s^{-1} in going from case B to case C. The cause is a nearly vertical segment in the difference spectra near 1266 Å due to spike in the flux spectrum at epoch 2. This artifact is included in the region covered by the case B analysis, but not by the case C analysis. We chose the spectral region of case C specifically to exclude such questionable features.

We adopt the radial velocity differences determined from case C as the best estimate of the actual orbital velocity differences. The B star radial velocity, V_i^{B}, at epoch i is (see, for example, Green 1985)

$$V_i^{\mathrm{B}} = V_0 + K_2[\cos(v_i + \omega_2) + e \cos \omega_2] \, , \tag{8}$$

where V_0 is the systemic velocity, K_2 is the semiamplitude of the B star secondary, e and ω_2 are the eccentricity and longitude of periastron (of the B star secondary), respectively, and v_i is the true anomaly at the observation epoch i. Then, the velocity difference between two epochs i and j,

$$\Delta V_{ij}^{\mathrm{B}} = V_i^{\mathrm{B}} - V_j^{\mathrm{B}} = K_2[\cos(v_i + \omega_2) - \cos(v_j + \omega_2)] \, , \tag{9}$$

depends explicitly only upon K_2 and ω. There remains a weak implicit dependence on the orbital elements since the independent variable of observation is the time, or orbital phase, which must be transformed into the true anomaly v using Kepler's equation. The radial velocity differences

TABLE 4

RADIAL VELOCITIES FROM DIFFERENCE SPECTRA

Variable	Fit A (km s^{-1})	Fit B (km s^{-1})	Fit C (km s^{-1})	ΔV_{ij}^{0} (km s^{-1})	Fit C′ (km s^{-1})
$\Delta V_{16}^{\mathrm{B}}$	57.35	57.64	56.80	−3.50	53.30
$\Delta V_{26}^{\mathrm{B}}$	43.83	42.17	38.52	−0.30	38.22
$\Delta V_{12}^{\mathrm{B}}$	15.14	15.67	18.43	−3.20	15.23
$\Delta V_{13}^{\mathrm{B}}$	16.04	14.69	16.09	+0.79	16.88
$\Delta V_{23}^{\mathrm{B}}$	−0.93	−2.46	−2.77	+3.99	+1.22
$\Delta V_{36}^{\mathrm{B}}$	41.30	43.99	41.28	−4.29	36.99
C_{126}	−1.62	−0.20	−0.15	0	−0.15
C_{123}	+1.83	+1.48	+0.43	0	+0.43
C_{236}	+3.46	+0.64	+0.01	0	+0.01
C_{136}	+0.01	−1.04	−0.57	0	−0.57
$\bar{C}$	+0.92	+0.22	−0.07	0	−0.07
$\sigma(C)$	1.91	0.94	0.36	0	0.36
$\sigma(\Delta V^{\mathrm{B}})$	1.10	0.54	0.21	0	0.21

TABLE 5

RADIAL VELOCITY SOLUTION FOR CASE C

	ΔV_{ij}^{B}		
EPOCHS	Observed (km s^{-1})	Solution (km s^{-1})	Observed − Solution (km s^{-1})
1–6	56.80	56.57	0.24
2–6	38.52	41.38	−2.86
1–2.........	18.43	15.18	3.25
1–3.........	16.09	18.20	−2.12
2–3.........	−2.77	3.02	−5.79
3–6	41.28	38.36	2.92
rms......	...	...	3.30

found from the GHRS observations are fitted to the functional form of equation (9), with K_2 and ω left as free parameters to be determined. The PHYSICA code of Chuma, Bennett, & Kost (1996) was used throughout the analysis for least-squares fitting. The result is a rather poor fit yielding $K_2 = 29.9 \pm 1.9$ km s^{-1}, $\omega_2 = 152\overset{\circ}{.}0 \pm 4\overset{\circ}{.}7$, and $\sigma_{\rm rms} = 3.4$ km s^{-1}. A comparison of the velocities predicted from this fit with the observed ΔV_{ij}^{B} values is given in Table 5.

The G160M spectra of the 1245–1285 Å region were all preceded by a wavelength calibration. The expected precision of about 0.2 diode (Soderblom et al. 1994) corresponds to about 3.5 km s^{-1} at 1260 Å. This is consistent with the scatter about the fitted radial velocity curve and suggests that zero-point errors in the wavelength calibration might dominate the systematic errors. Note that the previous check sum calculation is unaffected by the presence of wavelength calibration errors since the net contribution to the C_{ijk} check sums from calibration errors is identically zero. Then, we can write the observed radial velocities as

$$V_i^{B} = V_0 + K_2[\cos(v_i + \omega_2) + e\cos\omega_2] + V_i^0 , \quad (10)$$

where V_i^0 is the (unknown) zero-point error in the wavelength calibration for the spectrum observed at epoch i, and V_0 is the systemic velocity. The velocity differences between epochs are given by

$$\Delta V_{ij}^{B} = V_i^{B} - V_j^{B} = K_2[\cos(v_i + \omega_2) - \cos(v_j + \omega_2)] + \Delta V_{ij}^0 , \quad (11)$$

where $\Delta V_{ij}^0 = V_i^0 - V_j^0$, and the *corrected* velocity differences are

$$\Delta \tilde{V}_{ij}^{B} = \Delta V_{ij}^{B} - \Delta V_{ij}^0 = K_2[\cos(v_i + \omega_2) - \cos(v_j + \omega_2)] . \quad (12)$$

The value of ΔV_{ij}^0 can be estimated from the position of interstellar lines in the spectrum as follows.

TABLE 6

RADIAL VELOCITY SOLUTION FOR CASE C′

	$\Delta \tilde{V}_{ij}^{B}$		
EPOCHS	Observed (km s^{-1})	Solution (km s^{-1})	Observed − Solution (km s^{-1})
1–6	53.30	53.37	−0.07
2–6	38.22	38.96	−0.74
1–2.........	15.23	14.41	0.82
1–3.........	16.88	17.27	−0.39
2–3.........	1.22	2.86	−1.64
3–6	36.99	36.10	0.89
rms......	...	...	0.90

The spectral region 1245–1285 Å contains two C I lines near 1277 Å that are not observed to vary with orbital phase and have velocities and equivalent widths consistent with that expected from interstellar features. Wind models (Harper, Bennett, & Brown 1996) predict no low-velocity circumstellar contribution to these C I lines. Therefore, we assume these C I lines to be solely of interstellar origin and use these features to calibrate the zero-point shifts among the GHRS spectra observed at different epochs. While the absolute zero-point error in each spectrum is not found by this method, the differential zero-point errors are readily determined. A complete description of the procedure can be found in the Appendix; the differential zero-point corrections found are tabulated in the fifth column of Table 4. These corrections are seen to be consistent with the 3.5 km s^{-1} precision expected from the wavelength-calibrated G160M spectra.

Applying the zero-point corrections to the case C ΔV_{ij}^{B} values listed in the fourth column of Table 4, we obtain the corrected (case C′) values in the sixth column. We obtain the much improved radial velocity solution

$$K_2 = 28.2 \pm 0.6 \text{ kms}^{-1} , \quad (13)$$
$$\omega_2 = 152\overset{\circ}{.}2 \pm 1\overset{\circ}{.}4 ,$$
$$\sigma_{\rm rms} = 1.0 \text{ km s}^{-1}$$

for which χ^2 is reduced by a factor of 13 compared to case C. Radial velocities calculated from the case C′ solution are compared with the corrected $\Delta \tilde{V}_{ij}^{B}$ values in Table 6. The case C′ orbit solution yields a mass ratio of $M_{\rm B}/M_{\rm K} = K_1/K_2 = 0.83 \pm 0.02$, where we have used $K_1 = 23.35 \pm 0.14$ km s^{-1} from Griffin (1995). The value of ω_2 found is marginally consistent with the Griffin (1995) value of $\omega_2 = \omega_1 - 180° = 148\overset{\circ}{.}5 \pm 0\overset{\circ}{.}8$. We continue to use the Griffin value of ω in our analysis as it is based on a much larger data set and should be much better determined than our result.

Since the semiamplitudes K_j, $j = 1, 2$ can be expressed in terms of the orbital elements (Green 1985),

$$K_j = \frac{na_j \sin i}{\sqrt{1 - e^2}} , \quad (14)$$

we use the well-determined values of the eccentricity and mean motion $n = 2\pi/P$ to evaluate $a_1 \sin i$ and $a_2 \sin i$, where a_j is the semimajor axis of the orbit of component j around the center of mass. We find $a_1 \sin i = 2.86 \pm 0.02$ and $a_2 \sin i = 3.46 \pm 0.07$ in units of 10^8 km. The inclination i can not be determined solely from a radial velocity analysis.

3. LONG-BASELINE INTERFEROMETRY AND THE ECLIPSE LIGHT CURVE

3.1. *Introduction*

In this section, we use a combination of long-baseline interferometry (obtained with the Mark III optical interferometer) and published photometry of the eclipse and near-eclipse phases of ζ Aurigae to determine the absolute radius of the K supergiant primary and the absolute semimajor axis of the orbit. Photometry of the partial eclipse phases and the solution of the "visual orbit" found by interferometry provide independent determinations of the orbit inclination. With the inclination and mass ratio determined, the masses of both stars are found from Kepler's third law.

The eclipse photometry effectively provides a determination of $a/(R_K \cos \delta)$, where R_K is the K star radius, a is the orbit semimajor axis, and δ is the latitude of the eclipse chord (which determines i), from the eclipse duration P_{ecl} (see Fig. 2). Since the interferometry directly gives the ratio a/R_K, the eclipse latitude δ and the inclination i are determined. With i known, the orbit scale and the stellar masses are fully determined.

3.2. *Optical Interferometry*

ζ Aurigae was observed with the Mark III interferometer on 22 nights as part of a 3 yr long observing program of spectroscopic binaries selected from the catalog by Batten, Fletcher, & MacCarthy (1989). (A recent status report can be found in Hummel & Armstrong 1994.) Measurements of the stellar interference fringe contrast (visibility amplitude) as a function of time in one night on a given baseline (Earth rotation aperture synthesis) yield separation and position angle of the binary components, as well as their magnitude difference and diameters in the three passbands employed by the Mark III (centered at $\lambda\lambda$ 800, 550, 500 [450 nm in 1989], each about 25 nm in width). Initial estimates of the seven elements of the "visual" orbit were obtained by applying the Thiele-Innes method (see, e.g., Green 1985) to the relative component positions. The value for the period from spectroscopy was adopted for the fit, as it has a much greater precision than can be achieved with the available interferometric data. Final system parameters, including magnitude differences and the diameter of the K star, were fitted directly to the visibility data using a method described by Hummel et al. (1993). A more detailed description of the Mark III, as well as of the procedures used to calibrate and model the visibilities, has been given by Shao et al. (1988), Mozurkewich et al. (1991), and Armstrong et al. (1992).

Since the stellar disk of the K4 supergiant is significantly larger than the resolution limit of the Mark III on the longest baseline (which is 31.5 m in length, giving about 3 mas resolution at λ450 nm), we fitted the visibilities of this component with a limb-darkened disk model using formulae given by Hanbury Brown et al. (1974). We adopted a linear limb-darkening law for the brightness of a point at a wavelength λ, $I_\lambda(\mu) = I_\lambda(1)[1 - u_\lambda(1 - \mu)]$, with μ as the cosine of the angle between the normal to the surface at that point and the line of sight from the star to the observer. We obtained the coefficients u_λ from the tables of Van Hamme (1993) for a stellar model of $T_{eff} = 4000$ K and $\log g = 1.0$, for which $u_{Ic} = 0.625$, $u_y = 0.896$, and $u_b = 1.026$. The limb-darkened diameter is larger than the uniform disk diameter measured at 800 nm by about a factor of 1.06. The B star disk is not resolved; we adopted 0.2 mas for its diameter. The drop in the upper envelope of the visibility amplitude with increasing baseline length due to the extended nature of the K star disk is demonstrated in Figure 5.

The orbit of the B5 dwarf relative to the supergiant is shown in Figure 6. In the figure, a small arrow indicates the sense of revolution, and T denotes the periastron (with the straight solid line indicating the major axis). The large circle indicates the limb of the supergiant; the B5 dwarf is behind the supergiant east of the major axis. Mid-eclipse occurs at JD 2,438,386.0, which is consistent with the photometric result to within $0^d.5$. Relative binary positions (ρ, θ) and corresponding uncertainty ellipses were derived from the data of each night in order to indicate the amount and quality of the data and their weights. The uncertainty ellipses were computed as follows: we adopted the diameters and magnitude differences from the global fit and determined values for ρ and θ from the data of each night. The visibility uncertainties were scaled to normalize the reduced χ^2 of the fit to unity, and uncertainty ellipses were fitted to the locus of (ρ, θ) values where the total χ^2

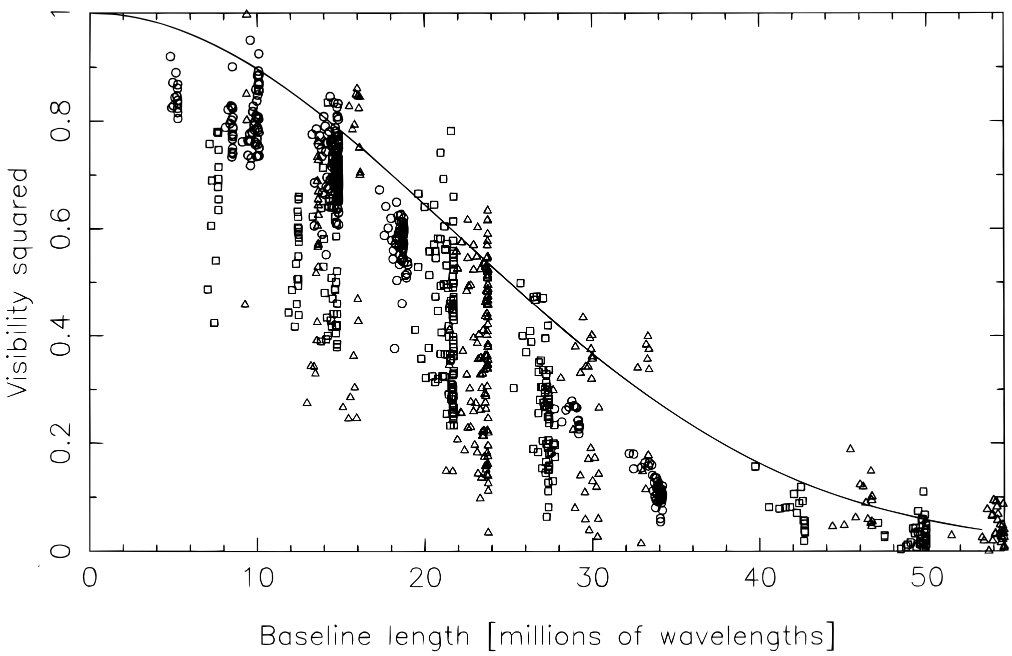

FIG. 5.—All measured visibility amplitudes plotted vs. the (projected) baseline length. Error bars are omitted for clarity. Open circles denote data of the red channel, open squares denote data of the green channel, and open triangles denote data of the blue channels. Solid line indicates upper envelope of visibilities computed for a model at 600 nm.

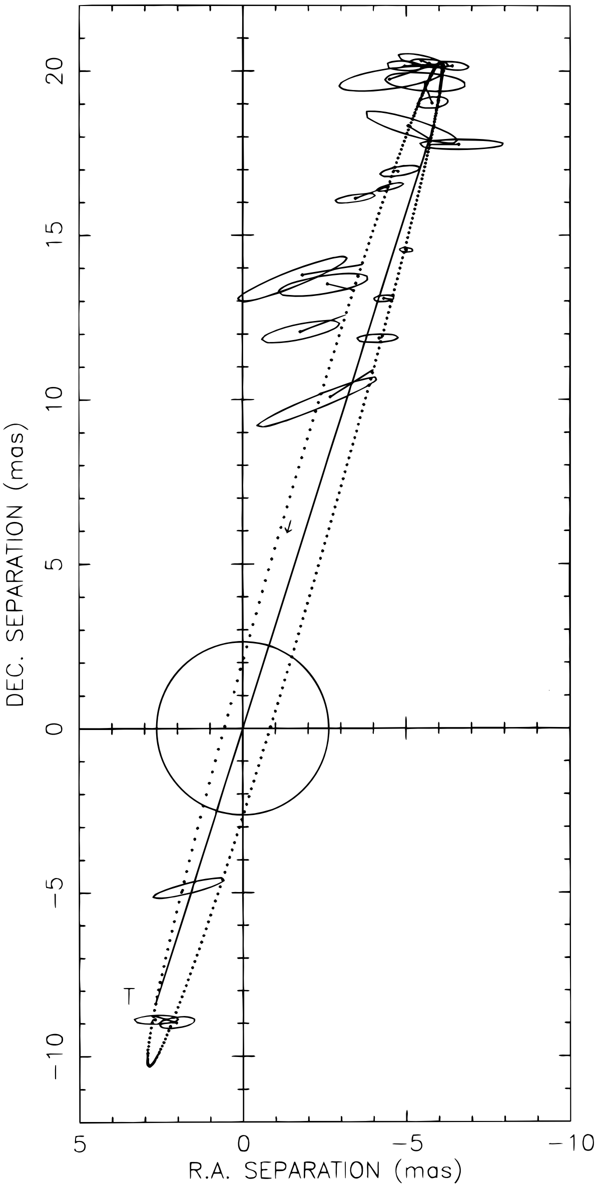

FIG. 6.—Orbit of ζ Aurigae projected on the sky. The K4 Ib primary star is at the center, and its limb is indicated by the large circle. The small dots are spaced by $P/360$, where P is the orbital period. North is up, and east is to the left. See text for further information.

increased by one over its minimum value (i.e., the number of visibilities). Table 7 lists the results; columns (1) and (2) give date and fractional Besselian year of the observation (at 8 UT), column (3) gives the length of the baseline, column (4) gives the number of scans, columns (5) and (6) give the separation and position angle (equinox = 1991.4) at 8 UT, columns (7)–(9) give the axes and the position angle of the uncertainty ellipse, and column (10) gives the deviation of the fitted relative binary position (ρ, θ) from the model values. Position angles are measured counterclockwise (over east) from north. We ask the reader to keep in mind that the orbital elements were not fitted to the listed binary positions, but to the visibilities as described in the last section.

Orbital elements and system parameters are listed in Table 2 (together with the results from spectroscopy by Griffin 1995). Uncertainties of the fit parameters were estimated as follows. First, the diagonal elements of the covariance matrix computed in the least-squares fit of the elements to the data provided formal uncertainties adopted as lower limits for the actual uncertainties. Second, uncertainties were increased over their lower limit if variations of the parameter values between fits to the data at various stages of the data calibration indicated that they were not as well defined as indicated by their formal uncertainty. The estimated uncertainties are supported by Monte Carlo simulations of data sets with artificial calibration errors, using a method described by Hummel et al. (1993). The interferometry on this system is of a somewhat lesser quality than could be obtained with the Mark III on systems where both components are unresolved. This is because short- to medium-length baselines with lower resolution had to be used in order to avoid the low visibility amplitudes occurring on long baselines due to the extended supergiant component. In addition, the projected orbit is narrow in the east-west direction which together with the east-west elongation of the positional uncertainty ellipses, due to the north-south orientation of the Mark III baselines, limits the precision of the inclination determination.

The Mark III observations yield a solution of the orbital elements in general agreement with the spectroscopic solution of Griffin (1995). Quantities derived from both sets of elements showed no significant ($>2\ \sigma$) deviations. The Mark III observations provide values of the orbital inclination angle i, the angular semimajor axis a, and the angular diameter D_K, unobtainable by purely spectroscopic means. The derived angular diameter of the K star (5.3 mas) is in good agreement with the value (5.5 $\pm$ 0.3 mas) found by Di Benedetto & Ferluga (1990) using infrared long-baseline interferometry.

3.3. *Eclipse Photometry*

The eclipse radius is not well defined since partial eclipse is mostly atmospheric rather than geometric. The behavior of the light curve during ingress or egress should allow the nature of the eclipse to be deduced, since the scale height over which the B star flux disappears is determined by the larger of the atmospheric scale height and the B star radius. However, nature has conspired that these two scales are similar in ζ Aurigae. Erhorn (1990) found the radius of the B star to be $R_B = 5.1\ R_\odot$ from a photometric analysis of the system. Eaton (1993), in his study of chromospheric absorption lines in the ultraviolet, found the scale height of the K star chromosphere to be about 6–8 $R_\odot$. These scales are so similar that we cannot expect to infer information about either scale reliably from the behavior of the light curve at partial eclipse. We determine the B star radius in § 4 by a completely independent technique using flux-calibrated GHRS observations.

We compiled published photometry of ζ Aurigae (for sources, see Table 8) and initially calculated the orbital phases (from mid-eclipse) using the ephemeris of Wood et al. (1980). In the course of fitting the light curves it was found that the alignment of data from different eclipses, particularly the rapidly varying portions during partial eclipse, was considerably improved by a modification of the Wood ephemeris. Therefore, we adopted the revised ephemeris

$$\mathrm{HJD(Obs.)} = 2{,}438{,}386.540 + 972.183 \times \mathrm{Phase}\ , \quad (15)$$

TABLE 7

MARK III OBSERVATION AND RESULT LOG FOR ζ AURIGAE

UT Date (1)	Besselian Year (−1900) (2)	Baseline (m) (3)	Number of Scans (4)	ρ (mas) (5)	θ (deg) (6)	σ_{maj} (mas) (7)	σ_{min} (mas) (8)	φ (deg) (9)	$O-C$ (mas) (10)
1989 Oct 14	89.7857	8.2	12	20.25	347.19	1.63	0.31	98.1	1.99
1989 Oct 19	89.7994	15.2	6	20.75	346.23	0.56	0.14	86.9	1.40
1989 Oct 27	89.8213	15.2	10	21.02	344.23	0.58	0.12	84.5	0.58
1989 Oct 28	89.8240	15.2	10	21.04	344.95	0.73	0.15	78.6	0.79
1989 Nov 1	89.8350	15.2	13	21.15	342.35	0.50	0.12	85.3	0.28
1989 Dec 5	89.9281	8.2	11	19.89	343.06	0.48	0.17	96.1	0.75
1989 Dec 8	89.9363	4.3	14	20.44	344.14	1.24	0.27	86.1	0.32
1990 Sep 14	90.7029	15.4	10	5.26	159.36	1.14	0.16	104.0	0.79
1990 Oct 24	90.8124	27.6	18	9.21	167.17	0.56	0.17	97.5	1.06
1990 Oct 26	90.8179	27.6	25	9.28	163.15	0.69	0.14	91.7	0.59
1991 Oct 1	91.7488	8.2	9	10.44	345.08	2.00	0.20	111.9	2.01
1991 Oct 15	91.7871	6.9	20	12.59	340.62	0.65	0.12	92.4	0.60
1991 Nov 2	91.8364	15.2	16	13.77	341.70	0.32	0.09	94.1	0.68
1991 Nov 27......	91.9048	12.0	33	15.39	341.01	0.21	0.07	86.4	0.56
1992 Feb 1........	92.0855	12.0	7	18.96	339.59	1.31	0.15	90.4	0.77
1992 Feb 5........	92.0965	12.0	13	19.02	344.57	1.50	0.25	73.5	0.96
1992 Oct 8........	92.7700	12.0	24	17.60	344.33	0.63	0.14	99.5	0.38
1992 Oct 17	92.7946	23.6	16	16.49	347.91	0.65	0.11	98.5	1.50
1992 Oct 18	92.7974	12.0	21	17.04	344.90	0.44	0.08	104.2	0.44
1992 Nov 22......	92.8932	8.2	13	13.91	352.45	1.82	0.24	111.3	2.28
1992 Dec 2	92.9206	12.0	6	13.76	349.12	1.39	0.27	99.0	1.18
1992 Dec 11	92.9452	12.0	21	12.20	351.68	1.23	0.23	101.9	1.97

where the orbital phase is measured from mid-eclipse, for all of the modeling of the eclipse photometry. The changes from the Wood ephemeris are very small, amounting to an increase of 0.019 d in the period, and an increase of 0.015 d in the time of mid-eclipse. The relative flux F_i in bandpass $i = U$, B, and V was calculated from the apparent magnitude m_i using the formula $F_i = -2.5 \log m_i$. The magnitude scale zero-point terms have been taken as zero for convenience since the absolute flux values are not needed for the present analysis.

We proceeded to fit the light-curve fluxes during the partial eclipse phases by an analytic function of the form

$$F(\phi) = F_{\max} \exp\left[-\exp\left(-\frac{|\phi| - \phi_0}{h}\right)\right], \qquad (16)$$

where ϕ is the orbital phase measured from mid-eclipse. This expression is motivated by a schematic picture of transmission through an extended atmosphere. The outer exponential represents the density variation of the atmosphere, while the inner exponential reflects the dependence of transmitted flux on optical depth. We find that this simple function provides a good fit to a compilation of photometric observations from the literature for the U, B, and V bands. We have used the absolute value of the orbital phase in the function since we found no significant difference between the egress light curve and the ingress light curve reflected about mid-eclipse. The light curves and analytic fits for the UBV photometric bands are shown in Figures 7*a*, , 7*b*, and 7*c*.

TABLE 8

SOURCES OF ζ AURIGAE UBV PHOTOMETRY

Source	Eclipse Dates
Grant & Abt 1959	1955–1956
Kiyokawa 1967....................................	1963–1964
Lovell & Hall 1973	1971–1972
Sanwal, Parthasarathy, & Abhyankar 1973......	1971–1972
Shao 1964..	1963–1964
van Genderen 1964	1963–1964

Ideally, we should define the photometric K star radius, R_K, to be the radius of tangential optical depth unity in a spectral region (e.g., the V band) similar to that used for the interferometric observations in order that the photometric radii be directly comparable to the interferometric radii. However, this is very difficult to accomplish in practice, especially at V, since to reach unit tangential optical depth requires following the light curve through a decline of 1.09 mag from the out-of-eclipse brightness. But second contact is reached after a decline of only 0.15 mag at V, and so determining the radius of unit (tangential) optical depth would require a large extrapolation of the light curve beyond this point. Clearly, such an extrapolation can not be recommended. The same problem occurs for the B light curve, and it is only at U that unit tangential optical depth is reached before the K star flux dominates.

Therefore, we adopt the photometric radius of the K star to be the separation of the centers of the two stars at second (and third) contacts. We do not add a correction for the width of the partial phase, which would be appropriate if the eclipse were truly geometric in nature. The eclipse is atmospheric, i.e., the light curve is due to the gradual extinction of the light as a result of the increasing optical thickness of the line of sight and is not due to the geometric eclipse of the secondary star by a sharp edge. From our modeling of the chromospheric structure (Harper et al. 1996), we have found that the attenuation of flux during the partial phases is entirely due to spectral line absorption, largely from Fe II. The optical depth of the line of sight at second contact is still much less than unity (except at U), and so the adopted photometric radii will overestimate the actual interferometric radii.

This definition of the photometric radius, although not ideal from a theoretical perspective, is convenient since it is essentially invariant over the UBV spectral region. This result appears to be a coincidence resulting from competing

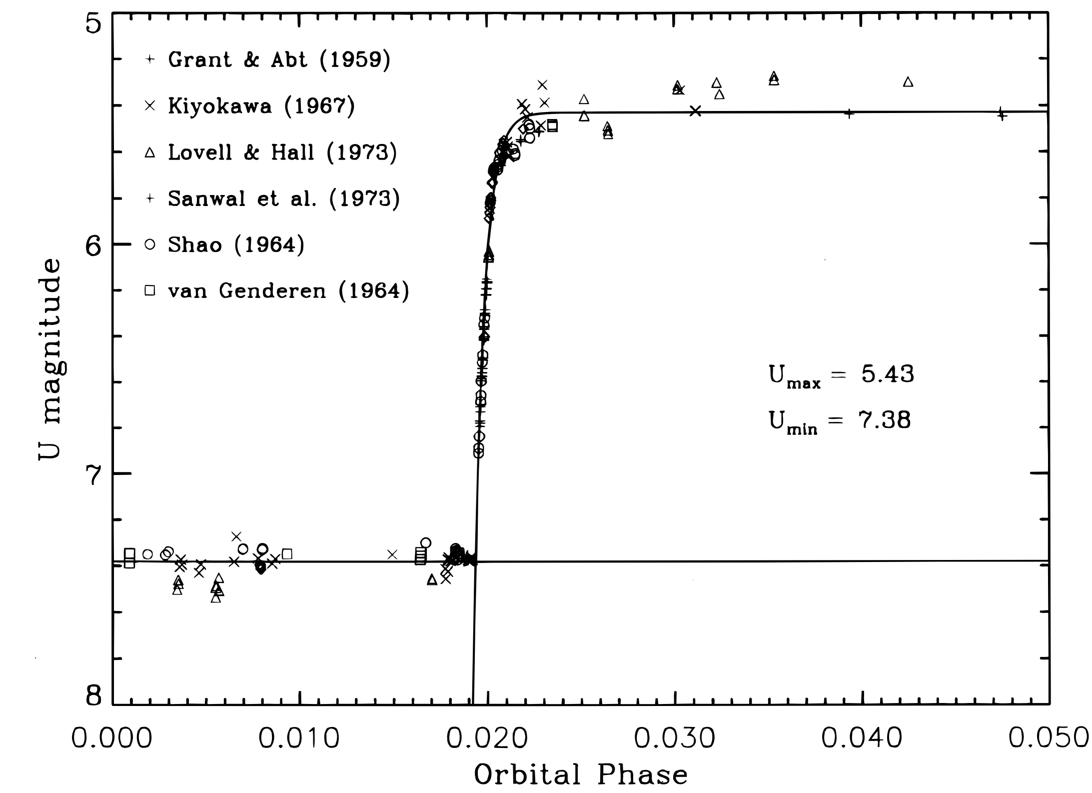

FIG. 7*a*

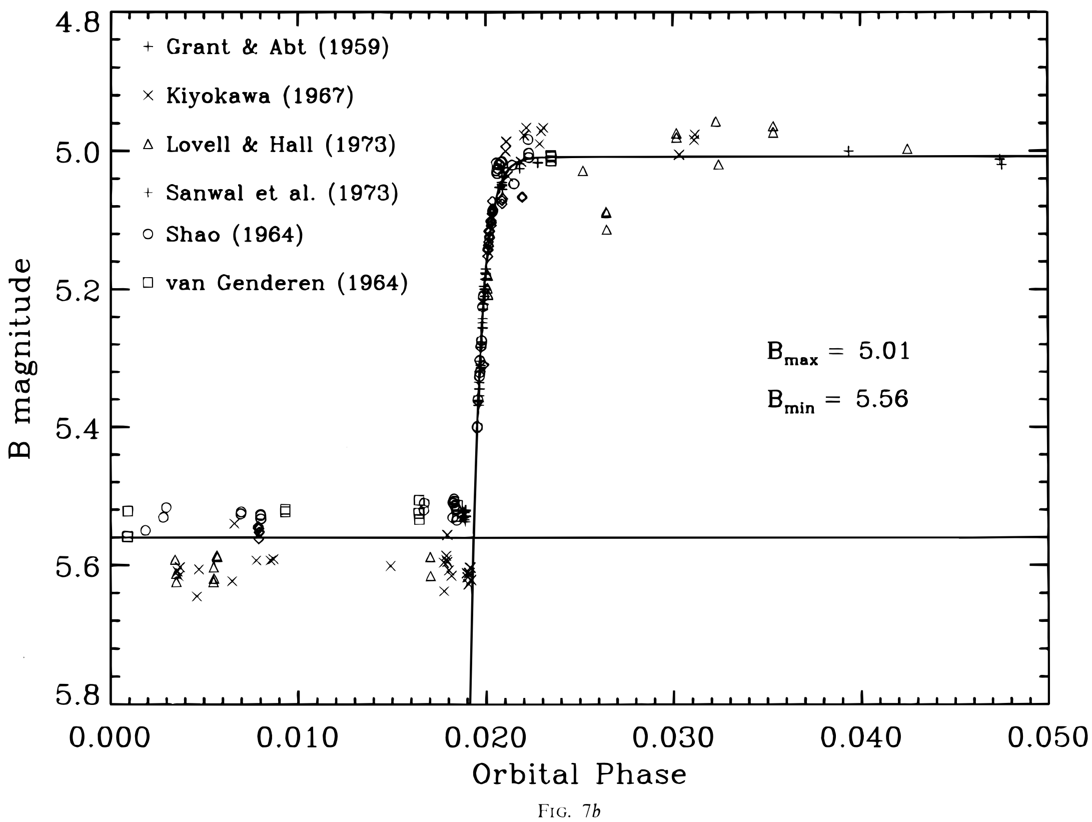

FIG. 7*b*

FIG. 7.—*UBV* light curves of ζ Aurigae near eclipse, compiled from the photometry of Grant & Abt (1959); Kiyokawa (1967); Lovell & Hall (1973); Sanwal, Parthasarathy, & Abhyankar (1973); Shao (1964); and van Genderen (1964). Phases are computed from the ephemeris: HJD(Obs.) = 2,438,386.540 + 972.183 × Phase. The ingress phases have been folded onto the egress phases to yield this combined light curve since the individual ingress and egress curves do not differ significantly. The solid line represents a fit to the light curve during partial eclipse, using the analytic expression given in the text. A line at constant magnitude is used to fit the flux during total eclipse. The out-of-eclipse and total eclipse magnitudes are given for each light curve. (*a*) *U* light curve, (*b*) *B* light curve, and (*c*) *V* light curve.

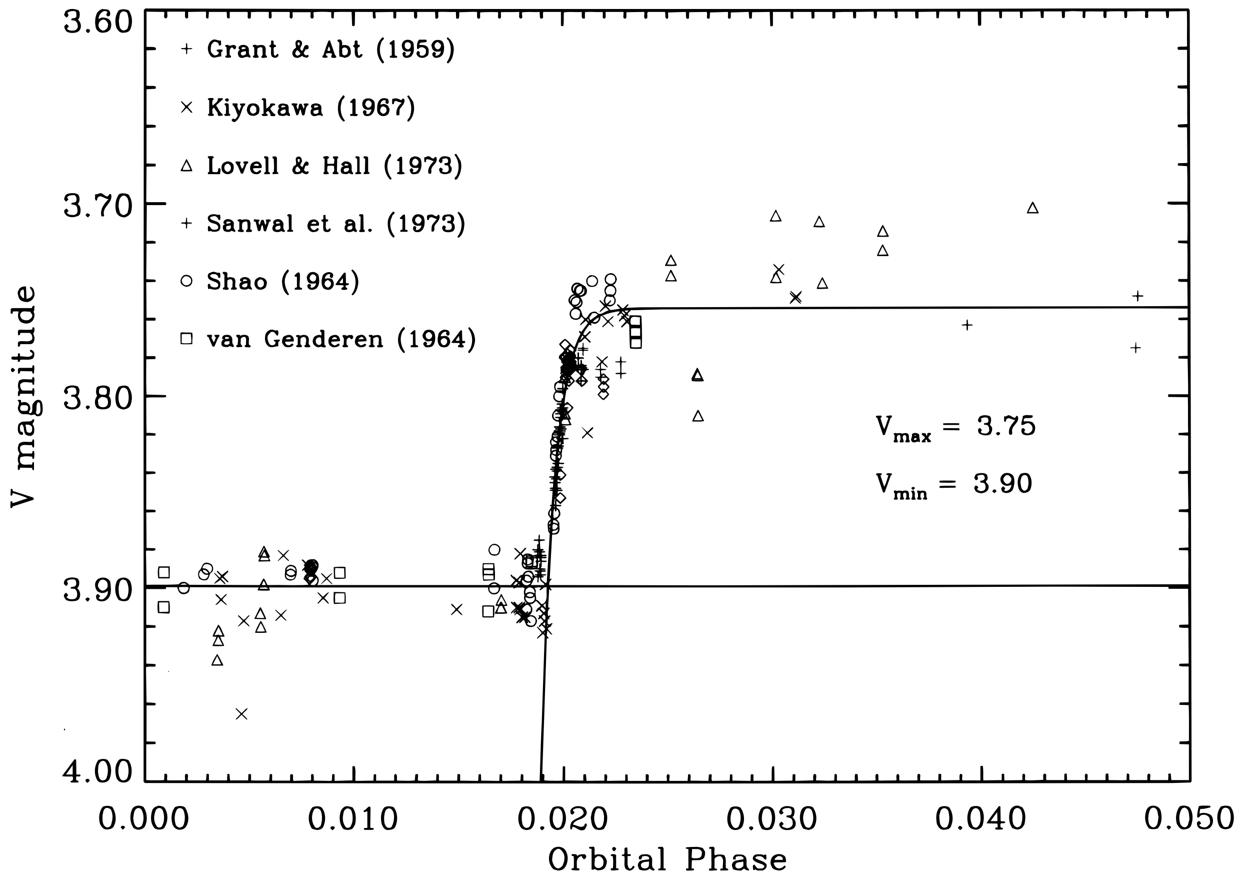

FIG. 7c

wavelength-dependent effects: (1) the decline of the light curve at shorter wavelengths occurs further from mid-eclipse, because of the greater chromospheric opacity at shorter wavelengths; and (2) the light curve displays a deeper minimum in total eclipse at shorter wavelengths, because of the much smaller contribution of K star flux. We denote the phase at third contact contact by $\phi_{\rm ecl}$ and note that, by inspection of the eclipse light curves (Fig. 7),

$$\phi^V_{\rm ecl} = \phi^B_{\rm ecl} = \phi^U_{\rm ecl} = 0.0193 \pm 0.0002 \; . \quad (17)$$

Hereafter, we will use the terms "ingress" and "egress" to refer to the orbital phases at second and third contact respectively, i.e., where $\phi_{\rm ecl} = \pm 0.0193$, and we define the eclipse duration by $P_{\rm ecl} = 2\phi_{\rm ecl} P$, where P is the orbital period. The true anomalies at ingress and egress are $v_{\rm ingress} = 289^\circ.1$ and $v_{\rm egress} = 315^\circ.6$.

The fit of the combined photometric data to equation (16) also provides the out-of-eclipse flux (the combined K and B star fluxes). The mean of the total eclipse flux gives the K star flux alone. The UBV magnitudes of both stars as determined by this procedure are reported in Table 9. These results are consistent with the photometry presented in Table 3 of Griffin et al. (1990).

TABLE 9

ζ AURIGAE UBV MAGNITUDES AND COLORS

Star	U	B	V	$B-V$	$U-B$
K	7.38	5.56	3.90	1.66	1.82
B	5.62	6.01	6.01	0.00	−0.39
K+B......	5.43	5.01	3.75	1.26	0.42

3.4. *Stellar and Orbital Parameters*

We use equation (19.7) of Green (1985) to derive the expression for the relative velocity of the ζ Aur stars projected onto the plane of the sky (the transverse velocity V_t),

$$V_t = \frac{na}{\sqrt{1-e^2}} \{[\sin(v+\omega) + e \sin\omega]^2 + [\cos(v+\omega) + e\cos\omega]^2 \cos^2 i\}^{1/2} \; . \quad (18)$$

The ζ Aurigae system exhibits total eclipses that appear to be reasonably central, since the length of the chord inferred from eclipse durations is not too different from the radius of the K star obtained by photometric modeling; see, e.g., Erhorn (1990) and the discussion in Griffin et al. (1990). This constraint restricts the inclination to be within about 6° of 90°, in which case $\cos^2 i$ is at most 0.01. Therefore, the second term in equation (18) may be neglected. We further define the transverse velocity amplitude,

$$K_t = \frac{na}{\sqrt{1-e^2}} \, , \quad (19)$$

by analogy with the expression for the radial velocity amplitudes K_1, K_2. Here a is the major axis of the relative orbit (in km for K_t in km s^{-1}). The transverse velocity then becomes

$$V_t = K_t[\sin(v+\omega) + e\sin\omega] \, , \quad (20)$$

an expression entirely analogous to the standard radial velocity formula (Green 1985) but with sine terms replacing the cosine terms. Note that V represents velocity, while v

denotes true anomaly, a standard but somewhat confusing notation when both terms appear together. We write the transverse velocity in this form because it conveniently separates the shape of the velocity curve, given by the accurately known expression within the square brackets of equation (20) that relies upon the well-determined orbital elements e and ω, from the amplitude K_t which depends on the value of a (which—until now—has been poorly known because of the difficulty of accurately determining K_2).

The latitude δ of the eclipse chord across the disk of the K star is related to the eclipse duration $P_{\rm ecl}$ by $\cos\delta = \langle V_t \rangle P_{\rm ecl}/2R_{\rm K}$, where $\langle V_t \rangle$ denotes the mean value averaged over the eclipse. By integration of equation (20), the mean transverse velocity during eclipse is found to be

$$\langle V_t \rangle = \frac{K_t}{\Delta v}\left[\cos\left(v_{\rm ingress} + \omega\right) - \cos\left(v_{\rm egress} + \omega\right)\right] + eK_t \sin\omega\ , \tag{21}$$

where $\Delta v = v_{\rm egress} - v_{\rm ingress}$, and $v_{\rm ingress}$, $v_{\rm egress}$ are the true anomalies at ingress and egress, respectively.

Substituting the values of $v_{\rm ingress}$ and $v_{\rm egress}$ into equation (21) and evaluating equation (19), we obtain $\langle V_t \rangle$ in terms of a. Using the Griffin (1995) orbital elements gives

$$\langle V_t \rangle = [(9.796 \pm 0.046) \times 10^{-8}\ {\rm s}^{-1}]a\ . \tag{22}$$

From this value of $\langle V_t \rangle$, the eclipse duration $P_{\rm ecl} = 37^{\rm d}.5 \pm 0^{\rm d}.4$, and $a/R_{\rm K} = 6.15 \pm 0.12$ determined from LBI (see Table 2), we find the eclipse transit latitude to be $\delta = 12^\circ.6^{+5^\circ.0}_{-10^\circ.0}$. The orbit inclination i is calculated from the geometric relation

$$\sin\delta = \frac{a\cos i}{R_{\rm K}}\left(\frac{1-e^2}{1+e\cos v_{\rm ecl}}\right) = \frac{a\cos i}{R_{\rm K}}\,(0.6948 \pm 0.0040)\ , \tag{23}$$

where $v_{\rm ecl} = -\omega - \pi/2 = 301^\circ.5 \pm 0^\circ.8$ is the true anomaly at mid-eclipse. The resulting inclination is $i = 87^\circ.0 \pm 1^\circ.3$. We note that this value, obtained by spectroscopic and photometric analysis, is in excellent agreement with the value of $i = 87^\circ.3 \pm 1^\circ.0$ found independently by interferometry.

We thereby obtain the absolute orbit dimensions $a_1 = 2.86 \pm 0.02$, $a_2 = 3.46 \pm 0.07$, and $a = a_1 + a_2 = 6.32 \pm 0.07$ in units of 10^8 km. From LBI measurements, the angular size of the orbit is known and therefore the distance to the system, $d = 261 \pm 3$ pc, follows immediately. Then, the LBI value of the K star angular diameter implies $R_{\rm K} = 148 \pm 3\ R_\odot$.

The sum of the stellar masses follows directly from Kepler's third law,

$$M_{\rm K} + M_{\rm B} = \frac{n^2 a^3}{G} = 10.6 \pm 0.2\ M_\odot\ , \tag{24}$$

where G is the gravitational constant, and $n = 2\pi/P$ is the mean motion. Using $M_{\rm B}/M_{\rm K}$ found from the radial velocity analysis, we obtain $M_{\rm K} = 5.8 \pm 0.2\ M_\odot$ and $M_{\rm B} = 4.8 \pm 0.2\ M_\odot$ for the individual stellar masses.

4. THE ULTRAVIOLET FLUX AND INTERSTELLAR EXTINCTION

We now proceed to determine the angular diameter $\theta_{\rm B}$ of the B star by scaling reddened synthetic spectra to fit the flux-calibrated GHRS observations. We examine the dependence of the angular diameters obtained by this procedure as a function of wavelength; clearly, a reasonable model for the star and reddening must not exhibit a dependence upon wavelength. We will use this requirement of a "flat" (i.e., zero slope) $\theta_{\rm B}(\lambda)$ relation to constrain the stellar parameters ($T_{\rm eff}$, log g) and reddening A_V consistent with the inferred stellar diameter.

The observed flux at the earth, $F_\lambda^{\rm obs}$, is related to the intrinsic flux at the stellar surface, $F_\lambda^{\rm intrins}$, by

$$F_\lambda^{\rm obs} = \tfrac{1}{4}\theta_{\rm B}^2 \times 10^{-0.4A_\lambda} F_\lambda^{\rm intrins}\ , \tag{25}$$

where $\theta_{\rm B}$ is the B star angular diameter in radians and A_λ is the interstellar extinction in magnitudes along the line of sight. Inverting, we can express the angular diameter of the star in terms of observed and intrinsic stellar fluxes, and the interstellar extinction, as

$$\theta_{\rm B} = 2\left(\frac{F_\lambda^{\rm obs}}{10^{-0.4A_\lambda} F_\lambda^{\rm intrins}}\right)^{1/2} \tag{26}$$

Then, using our flux-calibrated GHRS observations of ζ Aurigae to determine $F_\lambda^{\rm obs}$, and model fluxes computed by the SYNSPEC synthetic spectrum code of Hubeny (1988) to estimate $F_\lambda^{\rm intrins}$, we obtain an estimate of the B star angular diameter (for an assumed value of A_V). The SYNSPEC code actually computes H_λ, the first radiation moment or Harvard flux, which is related to the physical flux by $F_\lambda = 4\pi H_\lambda$. In this manner, we determined angular diameters $\theta_{\rm B}$ for each of 21 GHRS spectra covering the spectral region 1190–3130 Å by minimizing the least-squares residual from the computed model spectrum. Regions containing circumstellar and interstellar absorption lines were assigned zero weight in the fitting. We also computed angular diameters from the *UBV* broadband fluxes. We converted the B star magnitudes obtained from the eclipse photometry of § 3.3 to absolute fluxes using the calibrations of Allen (1976). The intrinsic stellar flux in each of the *UBV* bands was determined by integration of the synthetic spectrum over the filter response functions of Johnson (1965).

The interstellar extinction, A_λ, is calculated using the formulae of Cardelli, Clayton, & Mathis (1989, hereafter CCM). The CCM extinction law is a parameterization depending upon the visual extinction A_V and the total-to-selective extinction $R \equiv A_V/E(B-V)$. In the absence of any obvious peculiarities along the ζ Aurigae line of sight, we adopt the value of $R = 3.09$ found by Rieke & Lebofsky (1985). Then, the inferred angular diameters $\theta_{\rm B}$ depend only on the interstellar extinction A_V and the stellar effective temperature $T_{\rm eff}$ (we ignore the extremely weak dependence on stellar gravity).

Experimentation showed that a flat $\theta_{\rm B}(\lambda)$ relation can be found for each assumed $T_{\rm eff}$ through the choice of an appropriate A_V. Therefore, in an attempt to constrain the acceptable range of $T_{\rm eff}$ and A_V further, we computed the B star angular diameters using equation (26) for the 91 models on the 7×13 grid of ($T_{\rm eff}$, A_V) defined by

$$T_{\rm eff} = [13500, 14000, 14500, 15000, 15450, 16000, 16500]$$

and

$$A_V = [0.00, 0.04, 0.08, 0.12, 0.16, 0.20, 0.24, 0.28, 0.32, 0.36, 0.40, 0.44, 0.48]\ .$$

At each ($T_{\rm eff}$, A_V) grid point, we fitted a least-squares line through the (λ,$\theta_{\rm B}$) values and noted the value $\theta_{\rm B}(3000)$ at 3000 Å from this fit. The stellar photospheric models used to represent the intrinsic stellar flux of the B star were computed using the TLUSTY code of Hubeny (1988) for the above vector of $T_{\rm eff}$ values with log $g = 3.9$ (from Paper I). These models were computed with the bound-free continua of the levels of H and He I up to $n = 5$ (a total of 21 levels) computed in non-LTE (the non-LTE/C models of Paper I). Atomic lines were computed assuming LTE. All of the model computed for this study used solar abundances from Anders & Grevesse (1989). The synthetic spectra were computed using the SYNSPEC code of I. Hubeny. The line strengths of C I and Si II lines in the synthetic spectra were reduced as described in Paper I in order to mimic non-LTE effects in the observed spectra.

In Figure 8, we show a contour plot of the values of $\theta_{\rm B}(3000)$ on the ($T_{\rm eff}$, A_V) grid. We also plot the curve for which the slope of the fitted line is zero; this curve defines the locus of acceptable solutions in the ($T_{\rm eff}$, A_V) plane. From Figure 8, we see that this latter curve lies at nearly constant angular diameter $\theta_{\rm B} = 0.16$ mas, and thus the angular diameter is independent of $T_{\rm eff}$. Typical standard deviations of least-squares lines fit to the $\theta_{\rm B}(\lambda)$ points (near the zero-slope locus) are $\sigma \approx 0.01$ mas. Therefore, we adopt $\theta_{\rm B} = 0.16 \pm 0.01$ mas as our best estimate of the B star angular diameter, a result that is *independent of the adopted* $T_{\rm eff}$. Combining this result with the distance found in § 3.4 gives a stellar radius of the B star secondary of $R_{\rm B} = 4.5 \pm 0.3\ R_\odot$. Finally, using the mass of the B star from § 3.4, we obtain a value of the B star gravity of log $g_{\rm B} = 3.82 \pm 0.04$. This is in good agreement with the spectroscopic determination of log $g_{\rm B} = 3.9 \pm 0.1$ of Paper I.

We cannot obtain any additional temperature constraints from the flux analysis. However, we can use the spectroscopic constraints of Paper I on $T_{\rm eff}$ combined with the dynamically derived constraint on log g to further improve our estimate of $T_{\rm eff}$. Additionally, we now have G140L spectra of the entire Lyα profile of the secondary spectrum because of the availability of the GHRS Side 1 instruments following the *HST* COSTAR repair mission. We have therefore computed the root mean square residual $(\chi^2/N)^{1/2}$ between the observed and computed model spectra in the region of the diagnostic lines considered in Paper I for models computed on a grid of ($T_{\rm eff}$, log g). Here N is the number of pixels considered for each line. We use a grid given by

$$T_{\rm eff} = [13500, 14000, 14500, 15000, 15450, 16000, 16500]$$

and

$$\log g = [3.45, 3.65, 3.86, 4.00, 4.20, 4.40, 4.60] ,$$

and consider the line profiles of C III 1175 Å, Hε 3970 Å, He I 4026 Å, and H Lyα. For each line, we determine the values of log g that minimize the residual as a function of $T_{\rm eff}$. The resulting curve in the ($T_{\rm eff}$, log g) plane describes the locus

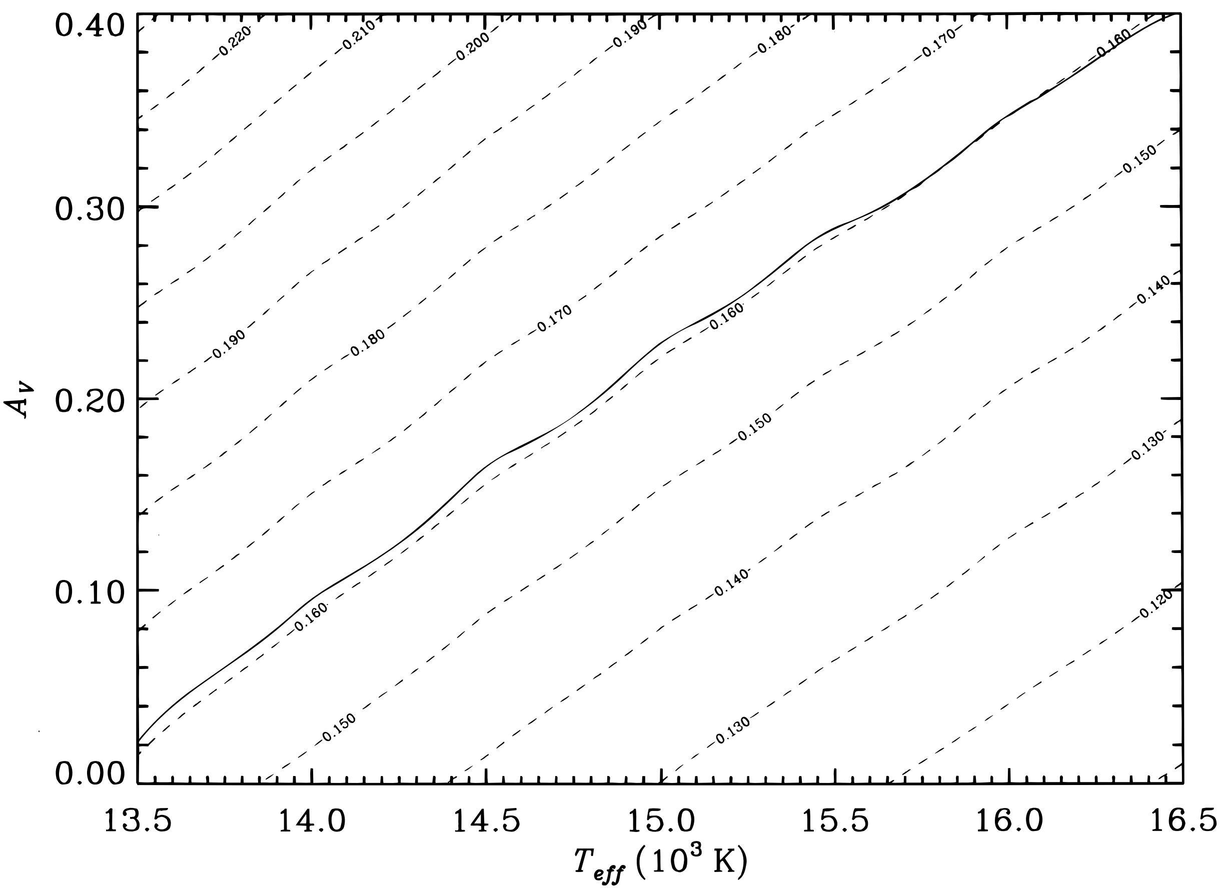

FIG. 8.—Contour plot in the (A_V, $T_{\rm eff}$) plane of the angular diameter (in mas) of the B star at 3000 Å. The angular diameter $\theta_{\rm B}$ is found for each flux-calibrated spectral region from equation (26), and a linear trend is fitted to obtain the wavelength-dependent $\theta_{\rm B}(\lambda)$ as described in the text. Realistic models require that the angular diameter $\theta_{\rm B}(\lambda)$ be independent of wavelength. This constraint is indicated by the solid curve that closely follows the 0.16 mas contour. Therefore, the angular diameter of the B star is $\theta_{\rm B} \approx 0.16$ mas, *independent of the choice of* A_V and $T_{\rm eff}$.

of models that provide the best fit to the observed line profile. For each line, we also plot bands of $\pm 2\ \sigma$ about these loci and superimpose these constraints onto a single plot in the ($T_{\rm eff}$, log g) plane. Finally, we add the constraint provided by the dynamically determined stellar gravity. The resulting plot appears as Figure 9 and, with the exception of Lyα that appears to be inconsistent, the intersections of the various constraints imply $T_{\rm eff} = 15200 \pm 200$ K. This result is consistent with the conclusions of Paper I, as expected since both determinations rely on the same spectroscopic data. The only new data used in Figure 9 are the discrepant Lyα profiles and the constraint on the stellar gravity provided by the more accurately determined stellar masses and radii found in this study.

From Figure 8, it then follows that $A_V = 0.25$ and $E(B-V) = A_V/R = 0.08$. In Figure 10, we show the B star angular diameters inferred from the UV fluxes for $T_{\rm eff}$(B star) = 15,200 K for differing values of the interstellar extinction along the line of sight. See Table 10 for spectral regions used for angular diameter fits. The angular diameters obtained from best-fitting extinction model of $A_V =$ 0.25 are shown in Figure 10*a*; it is seen that $\theta_{\rm B}(\lambda)$ does not depend significantly upon wavelength. The observations that are expected to be photometrically accurate are shown as filled symbols in this diagram. The outlier near 1700 Å is from observations made in order 33 of the GHRS Echelle-B. This is the shortest wavelength order available using

TABLE 10

Spectral Regions used for Angular Diameter Fits

Type of Observation	Epoch	Wavelength (Å)	Aperture
GHRS G160M	1	1190.5	SSA
GHRS G160M	1	1265.0	SSA
GHRS G160M	2	1265.0	SSA
GHRS G160M	3	1265.0	SSA
GHRS G160M	6	1265.0	SSA
GHRS G160M	1	1540.0	SSA
GHRS G160M	3	1572.0	SSA
GHRS G160M	6	1572.0	SSA
GHRS G160M	3	1643.0	SSA
GHRS ECH-B	2	1704.5	LSA
GHRS ECH-B	4	2150.0	LSA
GHRS ECH-B	1	2335.5	LSA
GHRS ECH-B	3	2335.5	LSA
GHRS ECH-B	1	2611.5	LSA
GHRS ECH-B	4	3003.0	LSA
GHRS ECH-B	4	3047.5	LSA
GHRS ECH-B	2	3074.0	LSA
GHRS ECH-B	3	3074.0	LSA
GHRS ECH-B	4	3130.0	LSA
GHRS G140L	7	1295.0	LSA
GHRS G140L	7	1575.0	LSA
U photometry	...	3531.9	...
B photometry	...	4352.8	...
V photometry	...	5440.4	...

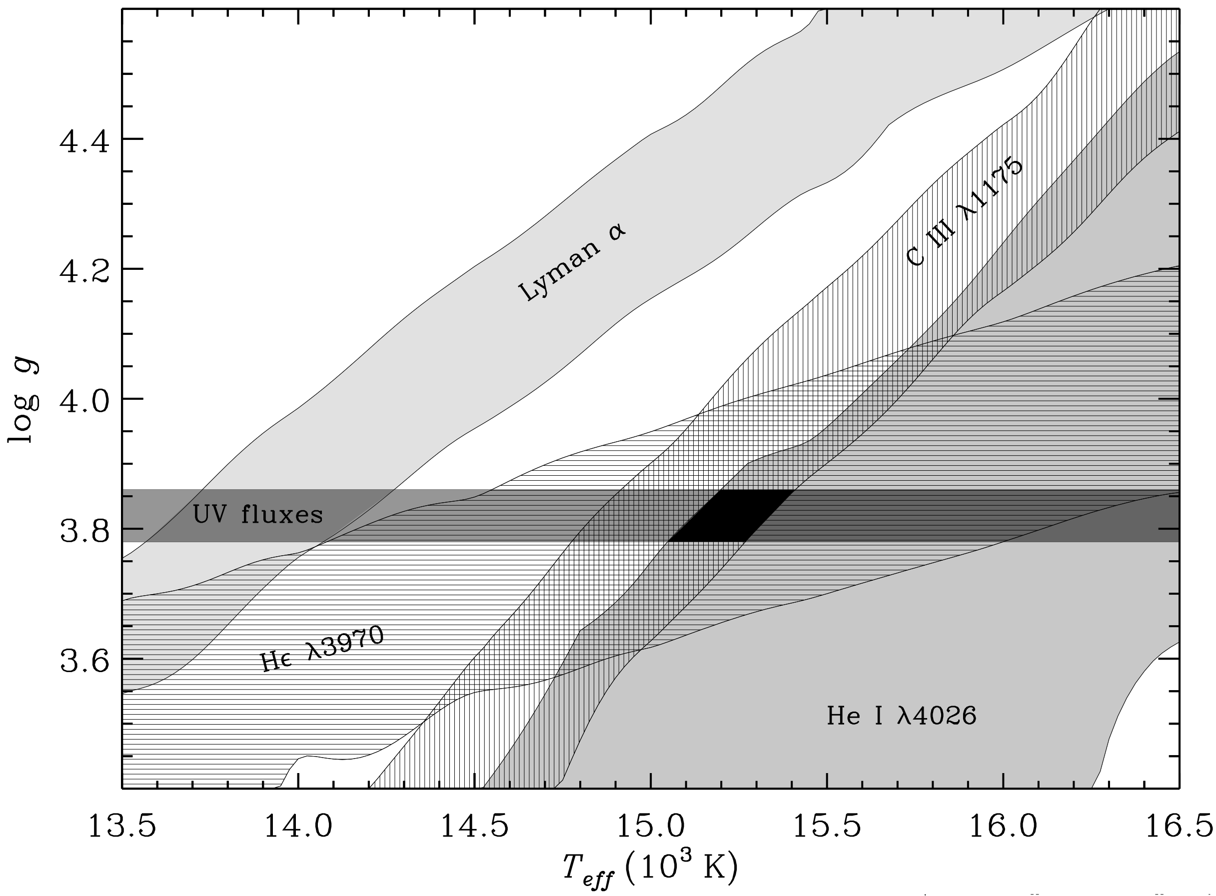

Fig. 9.—Constraints in the ($T_{\rm eff}$, log g) plane from line profile fits and stellar gravity determination. We show the regions where the theoretical line profiles lie within $\pm 2\ \sigma$ of the observed stellar profiles for Lyα, C III 1175 Å, Hϵ 3970 Å, and He I 4026 Å. The deviations are computed in a root mean square sense over the entire profile. The constraint of the B star gravity follows directly from the stellar mass and radius determinations as described in the text. The Lyα profile is clearly discrepant. The filled, black region is consistent with all of these constraints, with the exception of Lyα. The location of this intersection region implies $T_{\rm eff} = 15{,}200 \pm 200$ K.

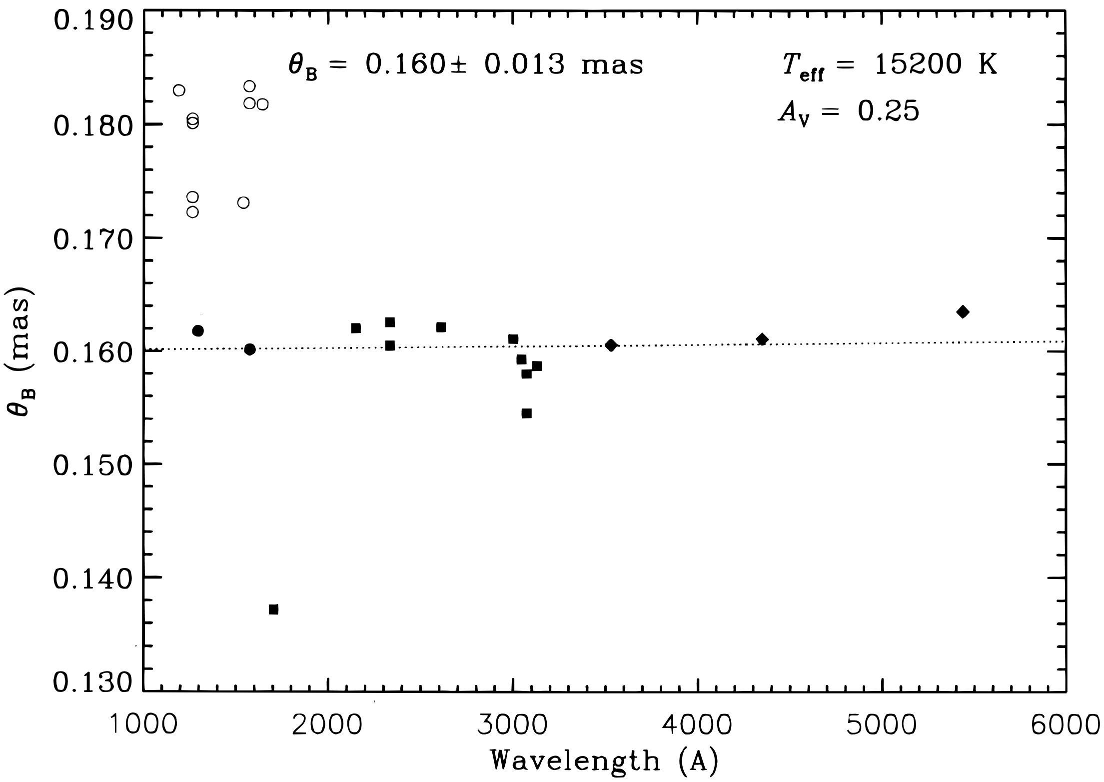

FIG. 10*a*

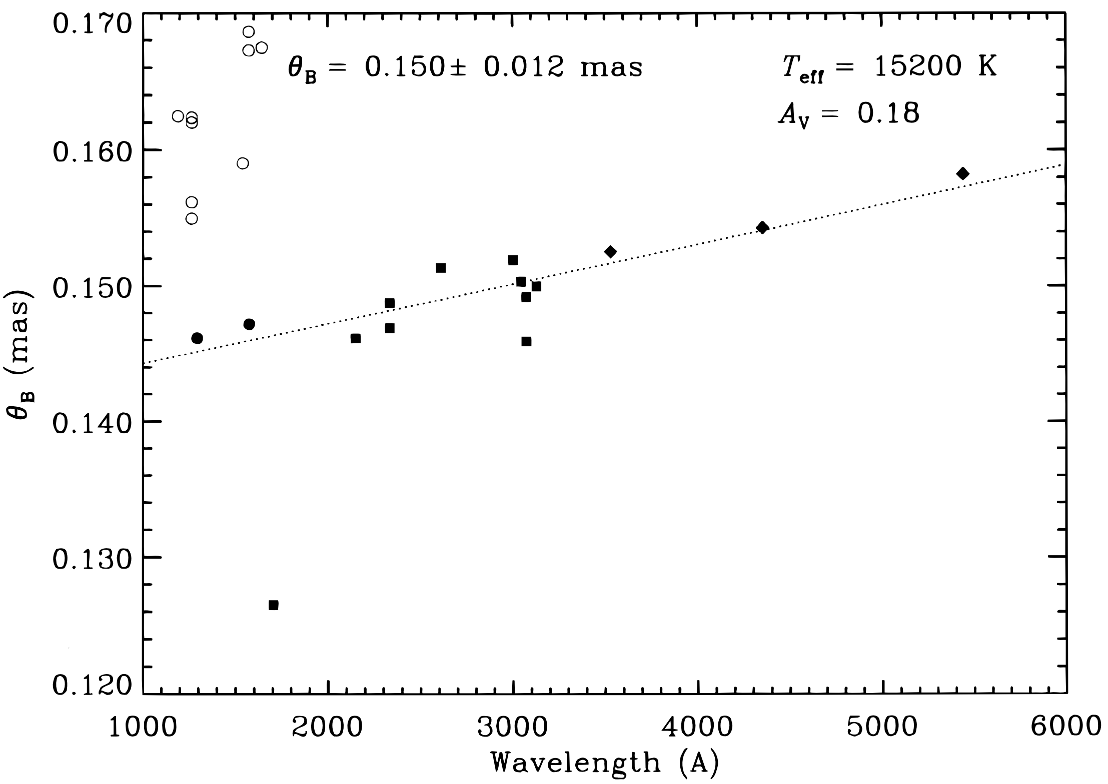

FIG. 10*b*

FIG. 10.—Angular diameters θ_B found for each of the spectral regions listed in Table 10 for different assumed values of the interstellar extinction. The black, filled symbols represent observations that should be photometrically accurate. In particular, circles denote low- and medium-resolution grating observations with the GHRS. Squares represent GHRS echelle observations, and the diamonds indicate *UBV* photometry. Filled symbols denote observations made through the GHRS Large Science Aperture, plus ground-based photometry, which should be photometrically reliable. Open symbols indicate observations made through the GHRS Small Science Aperture. The discrepant filled square near 1700 Å is apparently due to a poor calibration of order 33 of Echelle-B. The dashed line shows a least-squares fit to the filled symbols; the outlier at 1700 Å was excluded from this fit. The slope of the fitted line was evaluated in this manner for each (T_{eff}, A_V) grid point in Fig. 8 and used to deduce the zero-slope locus of physically realistic extinction models shown in that figure. (*a*) $A_V = 0.25$, (*b*) $A_V = 0.18$, and (*c*) $A_V = 0.32$.

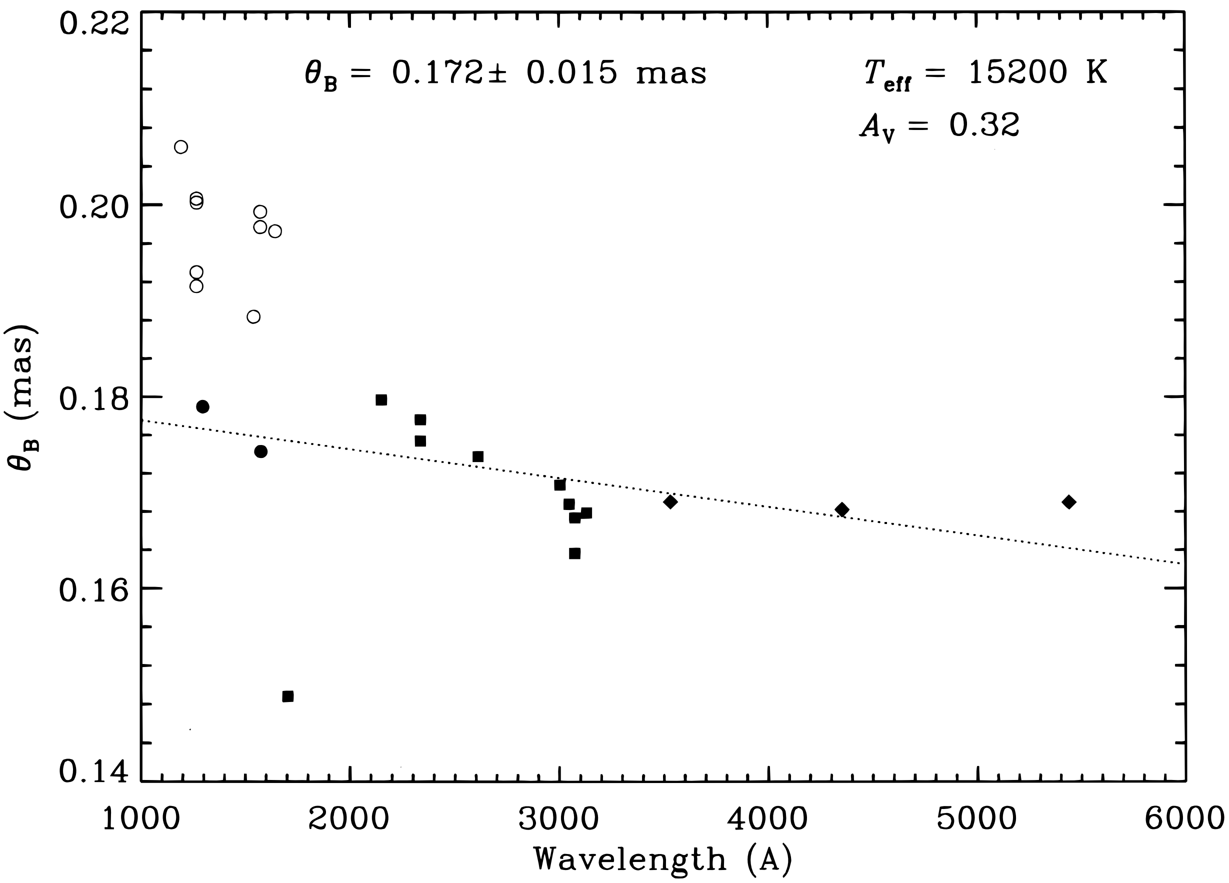

FIG. 10*c*

Echelle-B, and the flux calibration appears to be very poor. The calibration for this region has varied by more than a factor of 2 between *HST* Cycle 2 and Cycle 5. We have used a recent calibration in producing Figure 10*a*; use of the original Cycle 2 calibration would move the discrepant point almost as far above the mean trend as it presently is below it. We believe neither of these calibrations are accurate and have removed this point from the fit to the least-squares line to the $\theta_B(\lambda)$ points. A similar, but less extreme, problem occurs at the long wavelength end (orders 18 and 19) of Echelle-B. The cluster of points near 3000 Å in Figure 10*a* shows a significant deviation from the mean trend, and this is presumably due to the poorer quality of the flux calibration in this region. We have, however, retained these points in the fit to the mean trend of $\theta_B(\lambda)$. We also show similar figures for values of $A_V = 0.18$ (Fig. 10*b*) and $A_V = 0.32$ (Fig. 10*c*) in order to illustrate the sensitivity to the extinction model chosen. In both of these cases, a very definite trend of $\theta_B(\lambda)$ is present. The standard deviation from the mean trend is about $\sigma = 0.01$ mas in all cases. From the sensitivity of the slope of $\theta_B(\lambda)$ to A_V, we estimate that A_V can be reasonably determined to within ± 0.03. Therefore, we adopt $A_V = 0.25 \pm 0.03$ for the line of sight to ζ Aurigae. Then, $E(B-V) = A_V/R = 0.08 \pm 0.01$.

The computed Lyα profile differs substantially from the observed G140L profile of ζ Aurigae. In Figure 11*a*, we show the discrepancy between the predicted model Lyα profile for the stellar parameters of $T_{\rm eff} = 15{,}200$ K and $\log g = 3.82$ and the observed, high S/N spectrum obtained with the G140L low-resolution grating of the GHRS. Even the best-fitting model profile obtained for $T_{\rm eff} = 15{,}200$ K and $\log g = 4.35$ deviates significantly in shape from the observed profile, as shown in Figure 11*b*. However, this higher gravity is completely inconsistent with the value implied from the B star mass and radius. The entire region in ($T_{\rm eff}$, $\log g$) parameter space where a good match to the observed Lyα profile is obtained is inconsistent with the other spectroscopic diagnostics and the dynamical gravity (see Fig. 9). The Lyα profile is computed in SYNSPEC using a Stark-broadened profile supplied by Nicole Feautrier (unpublished), which differs only slightly from the standard Holtsmark profile. We are currently examining the reasons for the Lyα profile discrepancies. The results of that study will be published elsewhere.

An additional check of the consistency of the parameters can be made. The photometric analysis in § 3.3 provided *UBV* magnitudes of the K star primary. We obtained *RIJK* magnitudes and *IRAS* colors for ζ Aur from the SIMBAD database. These data are for the combined light of both stars, but the difference is negligible for the *IRAS* bands since the B star contributes little flux in these spectral regions. We corrected the *RIJK* magnitudes to account for the K star flux alone by assuming a B star magnitude of $m = 6.00$ for these bands. This correction is only approximate, but it suffices since the K star is several magnitudes brighter in the infrared, and so the flux correction is always very small (0.05 mag at R and less than 0.02 mag elsewhere). The K star magnitudes were then dereddened according to the adopted extinction model and, along with the *IRAS* fluxes, were converted to a F_λ flux scale and integrated over

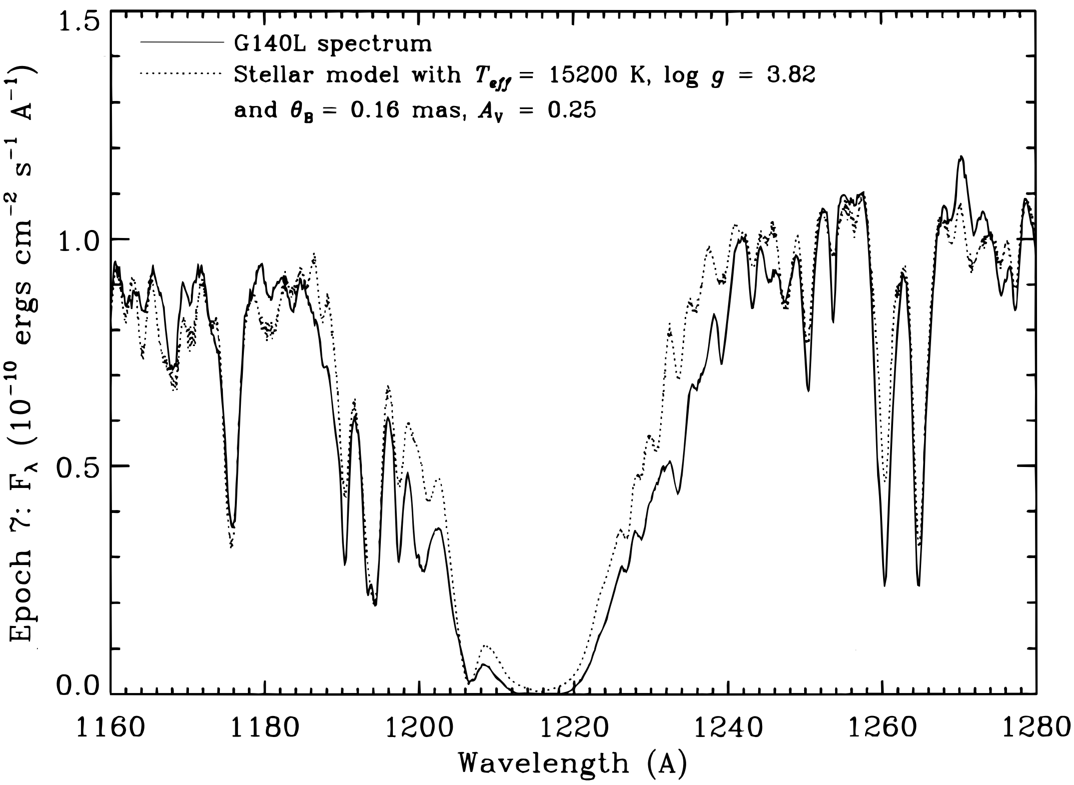

FIG. 11*a*

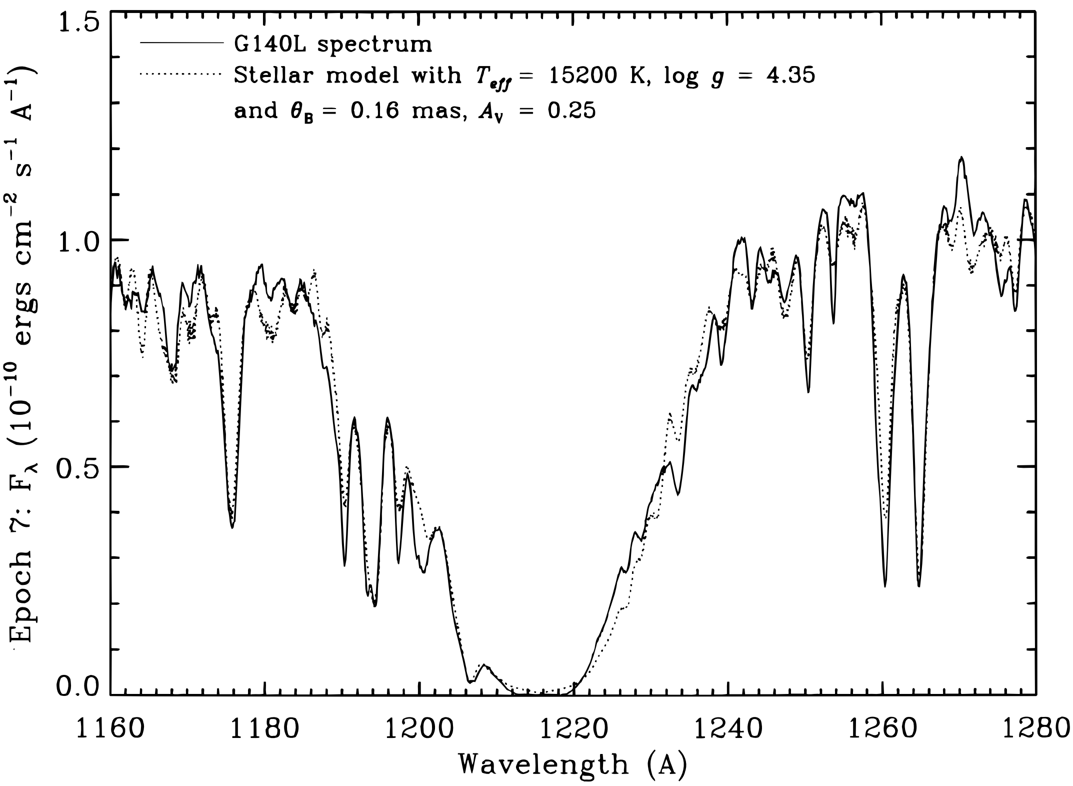

FIG. 11*b*

FIG. 11.—Profile of Lyα in ζ Aurigae with the G140L low-resolution grating of the GHRS (*solid curve*) compared to the theoretical line profile computed from various models. (*a*) The $T_{\rm eff} = 15{,}200$ K, log $g = 3.82$ model consistent with the other constraints (*dotted curve*). The Lyα profile is clearly inconsistent with the model. (*b*) The $T_{\rm eff} = 15{,}200$ K, log $g = 4.35$ model found by varying the stellar gravity to optimize the Lyα profile fit. The resulting gravity is completely inconsistent with that found from the stellar mass and radius (log $g = 3.82 \pm 0.04$). Even for this optimized fit, the theoretical profile deviates significantly from the observed Lyα spectrum.

wavelength to obtain the dereddened K star flux (at Earth), $F_{\rm dered} = (2.26 \pm 0.05) \times 10^{-6}$ ergs cm^{-2} s^{-1}. Then, using the angular diameter of the K star obtained from LBI, $\theta_{\rm K} = 5.27 \pm 0.10$ mas, we evaluated the effective temperature of the K star from

$$T_{\rm eff} = \left(\frac{4F_{\rm dered}}{\sigma\theta_{\rm K}^2}\right)^{1/4} = 3960 \pm 100 \text{ K} . \quad (27)$$

The dereddened flux spectrum of ζ Aurigae is shown in Figure 12. This effective temperature is in excellent agreement with the $T_{\rm eff} = 3920$ K obtained by McWilliam (1990) and the $T_{\rm eff} = 4000 \pm 150$ K found from the Nordic Optical Telescope (NOT) spectrum by Piskunov (1995). Therefore, we adopt $T_{\rm eff} = 3960 \pm 100$ K for the K supergiant primary of ζ Aurigae.

In conclusion, the overall good agreement of the dynamical and spectroscopic B star gravity, and the spectroscopic and bolometric $T_{\rm eff}$, suggests no major systematic errors are present in our analysis of the ultraviolet fluxes and interstellar extinction of ζ Aurigae.

5. POSITION ON THE H-R DIAGRAM

In this section we plot recent model evolutionary tracks for masses corresponding to the ζ Aurigae primary and secondary stars. We also plot the current position of these stars on the theoretical H-R diagram, using our estimates of the effective temperatures and luminosities. Since our determination of the stellar masses is independent of the determination of $T_{\rm eff}$ and L, agreement between the current positions and the evolutionary tracks on the H-R diagram provides a stringent test of overall self-consistency in this analysis. Additionally, since the ζ Aurigae primary and secondary are presumably coeval, the positions of these stars on the H-R diagram should lie on a common isochrone.

In Figure 13, we display evolutionary tracks of Schaller et al. (1992) and Bressan et al. (1993) for $Z = 0.020$ (approximately solar metallicity) and of Schaerer et al. (1993) and Alongi et al. (1993) for $Z = 0.008$. We have interpolated these various model tracks to correspond to the masses of the ζ Aur primary and secondary stars determined in § 2. These models all incorporate rather similar physics in their treatment of convective overshooting, assuming core overshooting distances in the range of 0.2–0.5 pressure scale heights. All of these models use the new OPAL radiative opacities of Rogers & Iglesias (1992) and Iglesias, Rogers, & Wilson (1992). The metallicity of $Z = 0.008$ corresponds to [Fe/H] $= -0.37$; these models are included to show the sensitivity of the calculations to the somewhat uncertain metal abundance of ζ Aurigae. Although we have assumed the metallicity to be solar in our model atmosphere computations, the compilation of McWilliam (1990) lists [Fe/H] $= -0.26 \pm 0.25$ for ζ Aurigae. We also indicate, by a shaded area in gray, the uncertainty in position of the model tracks due to the ± 0.20 $M_\odot$ errors in the determination of the stellar masses.

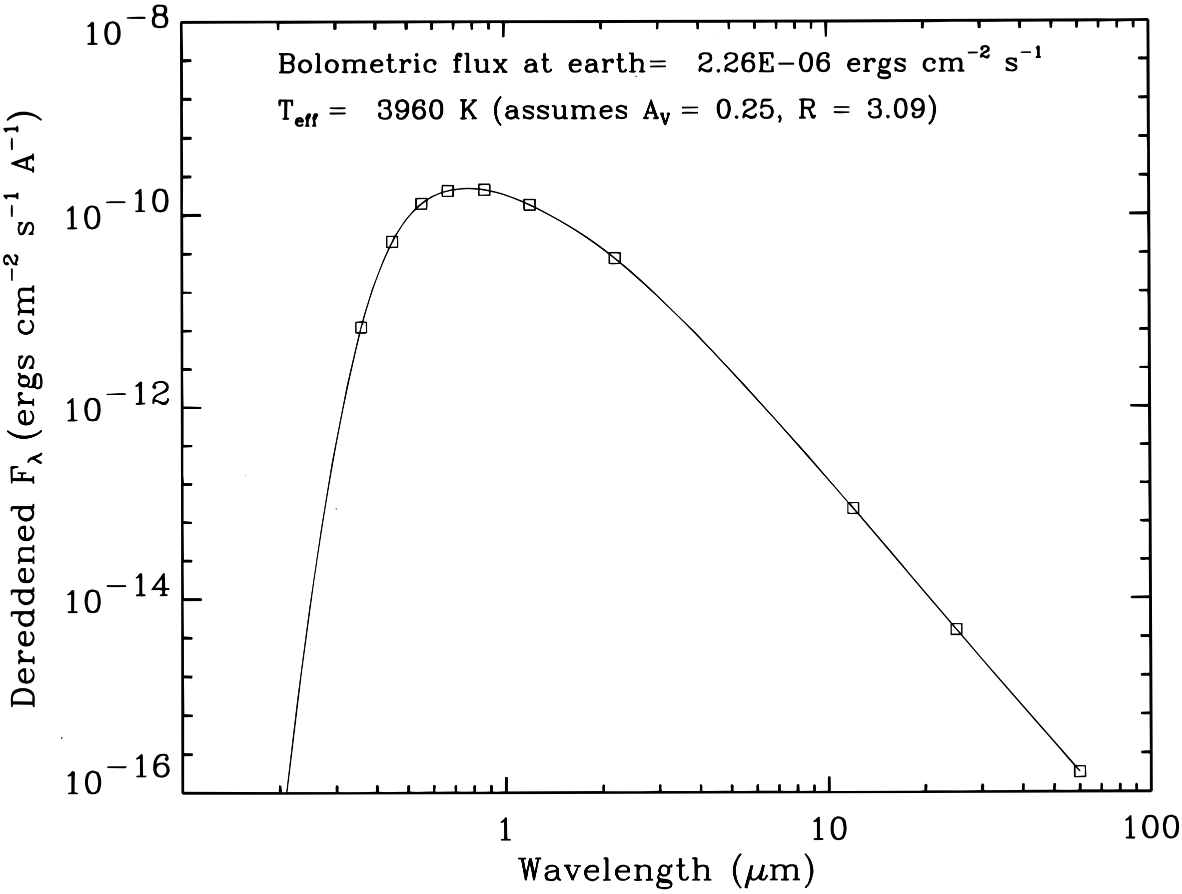

FIG. 12.—Dereddened flux of the K supergiant primary of ζ Aurigae at Earth. The squares are the *UBV* magnitudes found from eclipse photometry, *RIJK* infrared photometry from the SIMBAD database corrected for the B star flux as described in the text, and the *IRAS* fluxes at 12, 25, and 60 μm. The solid curve is a smooth interpolation of these flux points. The effective temperature, $T_{\rm eff} = 3960$ K, is a bolometric determination found from the integrated flux and the angular diameter observed with LBI.

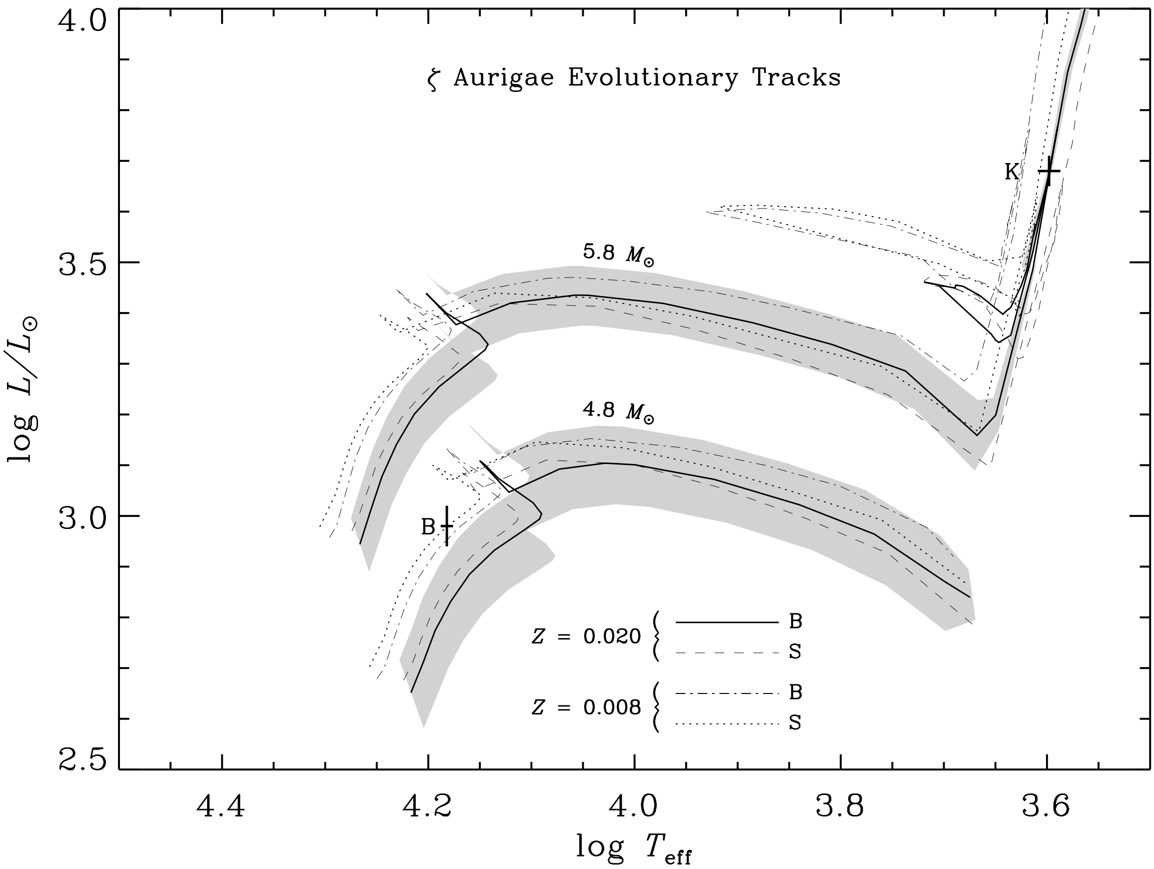

FIG. 13.—Evolutionary tracks for metal abundances of $Z = 0.020$ (solar) and $Z = 0.008$ are plotted on the theoretical H-R diagram. The tracks labeled B are from Bressan et al. (1993) for $Z = 0.020$ and Alongi et al. (1993) for $Z = 0.008$. The tracks labeled S are from Schaller et al. (1992) for $Z = 0.020$ and from Schaerer et al. (1993) for $Z = 0.008$. The areas shaded in gray show the uncertainty in the positions of the theoretical tracks of Bressan et al. (1993) due to errors of ± 0.20 $M_\odot$ in the stellar mass determinations. The shading in the region of the horizontal branch of the primary star track has been omitted for clarity. The positions of the ζ Aurigae K and B stars are marked by crosses, with the length of each arm indicating the ± 1 σ error.

It is evident from Figure 13 that the uncertainty in the location of the theoretical evolutionary tracks is dominated by the poorly determined metallicity and the error in the stellar mass determinations, rather than by differing physics of the various models. For the main sequence and Hertzsprung gap, the errors in the model track positions due to uncertainty in the metallicity are comparable to those resulting from uncertainty in the stellar masses. The errors from both effects are considerably larger than the scatter among the various models. However, for the giant branch, the location of the model tracks is insensitive to stellar mass, and the variation among the different models is comparable to the error due to the poorly determined metallicity. A better determination of the metallicity of ζ Aurigae is needed in order to further constrain the model evolutionary tracks.

We evaluate the luminosities of the primary and secondary stars, using the determinations of effective temperature and stellar radius presented in this analysis, to obtain log $L_K = 3.68 \pm 0.03$ $L_\odot$ and log $L_B = 2.98 \pm 0.04$ $L_\odot$. The resulting ($T_{\rm eff}$, $L/L_\odot$) points for both ζ Aurigae stars are also plotted on the H-R diagram of Figure 13. The positions of the individual stars are in good agreement with the evolutionary model tracks computed for our measured masses, and this suggests that no serious systematic errors are present either in our analysis of ζ Aurigae or in the recent theoretical model calculations.

In Figure 14*a*, we confirm that the ζ Aurigae primary and secondary stars are coeval by plotting the isochrones of Bertelli et al. (1994) for $Z = 0.020$ on the H-R diagram with the position of the two stars. The position of both ζ Aurigae component stars is consistent with an age of 70 Myr for $Z = 0.020$. Figure 14*b* shows the same figure but for the $Z = 0.008$ isochrones of Bertelli et al. (1994), implying a B star age of 93 Myr in this case. The K star position is somewhat inconsistent with the Bertelli et al. $Z = 0.008$ models. From Figure 13, it is evident that the $Z = 0.008$ model tracks of Schaerer et al. (1993) provide a good fit to the observed positions of both ζ Aurigae stars, but unfortunately, we do not have isochrones available for these models. Given the uncertainty in the metallicity, we adopt 80 ± 15 Myr for the age of ζ Aurigae.

The evolutionary status of the primary star is confused because of the presence of overlapping evolutionary tracks in the red giant region of the H-R diagram. The primary may be either on the first ascent of the red giant branch (RGB) or on its second ascent up the asymptotic giant branch (AGB), having already evolved around the horizontal branch blue loop. In the latter case, the age of the primary would be about 5×10^6 yr older. However, the lifetime on the lower AGB is quite short, and it is more likely that we are observing the primary on the upper RGB instead. Again, it would be very helpful to have a better metallicity determination for the system in order to con-

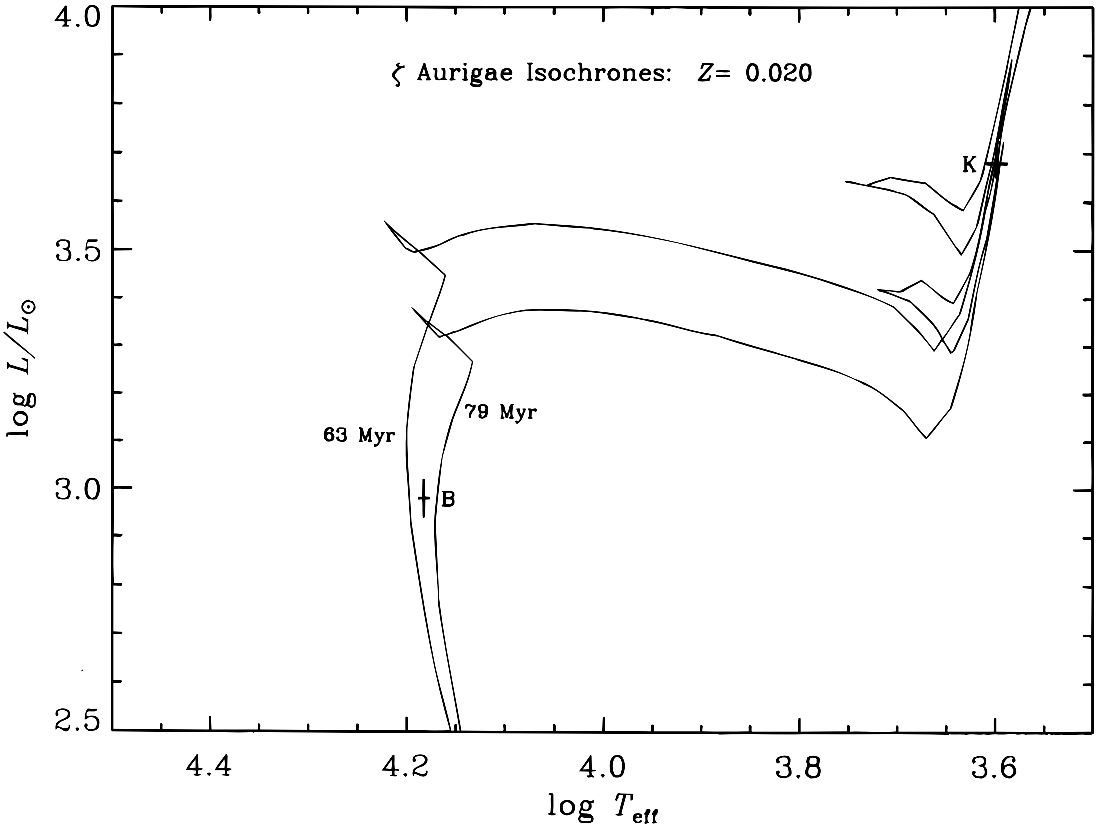

FIG. 14*a*

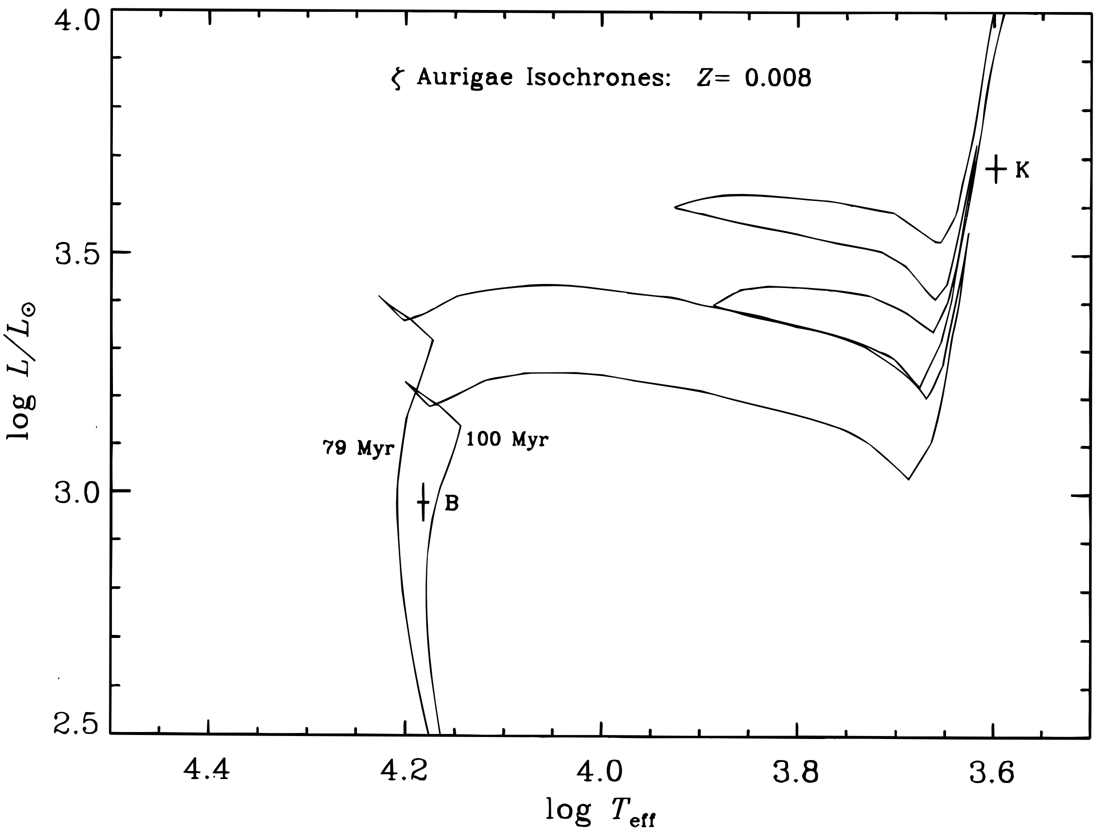

FIG. 14*b*

FIG. 14.—Isochrones of Bertelli et al. (1994) for differing metallicities are plotted on the theoretical H-R diagram, with the positions of the ζ Aurigae K and B stars superposed. The symbols for each star indicate the $\pm 1\ \sigma$ error bars. (*a*) $Z = 0.020$ (solar metallicity), and (*b*) $Z = 0.008$.

TABLE 11

SUMMARY OF ζ AURIGAE STELLAR & ORBITAL PARAMETERS

Quantity	K Star	B Star	System
T_{eff} (K)	3960 ± 100	15200 ± 200	...
log g	0.86 ± 0.02	3.82 ± 0.04	...
Radius ($R_\odot$)	148 ± 3	4.5 ± 0.3	...
Angular diameter (mas)	5.27 ± 0.10	0.16 ± 0.01	...
Mass ($M_\odot$)	5.8 ± 0.2	4.8 ± 0.2	...
Luminosity (log $L_\odot$)	3.68 ± 0.03	2.98 ± 0.04	...
Radial velocity amplitude (km s^{-1})	23.35 ± 0.14[c]	28.2 ± 0.6	...
Rotation velocity (km s^{-1})	8.5 ± 0.2[b]	200 ± 15[a]	...
Rotation period (days)	900 ± 40	1.1 ± 0.1	...
Age (10^6 yr)	80 ± 15	80 ± 15	80 ± 15
Orbital period (days)	...	...	972.183
Inclination, i (deg)	...	...	87.3 ± 1.0
Distance (pc)	...	...	261 ± 3
Extinction, A_V	...	...	0.25 ± 0.03
Reddening, $E(B - V)$	...	...	0.08 ± 0.01
Semimajor axis	a_1	a_2	a
(10^8 km)	2.86 ± 0.02	3.46 ± 0.07	6.32 ± 0.07
($R_\odot$)	411 ± 3	497 ± 10	908 ± 10
(R_K)	2.78 ± 0.06	3.36 ± 0.10	6.15 ± 0.12

[a] Bennett et al. 1995.
[b] Griffin et al. 1990, confirmed by Piskunov 1995.
[c] Griffin 1995.

strain the ages further. For now, we conclude that the primary star is probably still on the RGB.

6. CONCLUSIONS

We have determined the stellar mass, radius, and luminosity of ζ Aurigae A and B and have determined the semimajor axis of the orbit. We also have derived the distance to the ζ Aur system and the interstellar extinction along the line of sight. The results of our analysis are collected together in Table 11; the error estimates reported in this table are 1 σ errors. A significant advance reported here is an accurate value of the secondary star radial velocity amplitude K_2. Until now, K_2 has been poorly determined, and this uncertainty has been reflected in previously derived stellar masses and orbit dimensions (semimajor axis). Although further improvement in the accuracy of the determination of K_1 and K_2 is possible using precision radial velocity (PRV) techniques (see Campbell, Walker, & Yang 1988), the present mass determinations are sufficiently accurate to permit a meaningful comparison with model evolutionary tracks.

Plotting the ζ Aurigae primary and secondary stars on the H-R diagram provides a strong check on the self-consistency of our analysis and a stringent constraint on the theoretical models. The model tracks rely on masses based solely on the determination of the radial velocity amplitudes K_1, K_2, with only a very weak link to other observations through the sin i dependence. On the other hand, the positions of the stars in the H-R diagram depend upon the values of T_{eff} determined spectroscopically, and cross-checked for consistency with bolometric fluxes, and upon the stellar radii that are determined from long-baseline interferometry for the K star, and from flux-calibrated GHRS observations for the B star. We find good agreement between recent theoretical evolutionary tracks and the positions of both ζ Aurigae stars in the H-R diagram, although the poorly determined metallicity of the system contributes significant uncertainty to the position of the evolutionary model tracks in the H-R diagram. We find an age of 80 ± 15 Myr for the ζ Aurigae binary system. The overall self-consistency of the stellar and orbital parameters determined by a variety of observational techniques with the theoretical model calculations suggests the systematic errors in our analysis of ζ Aurigae (and in the theoretical models) are likely to be small.

This work was supported by NASA, under grants GO-3626.01-91A and GO-06069.01-94A from the Space Telescope Science Institute and by the Office of Naval Research. This research has made use of the SIMBAD database, operated at the CDS, Strasbourg, France. P. D. B. especially wishes to thank Roger Griffin for kindly supplying, and giving permission to quote, his recent orbit solution for ζ Aurigae prior to publication. We gratefully acknowledge the assistance of R. E. M. Griffin in providing an optical spectrum of ζ Aur B. P. D. B. also thanks I. Tuominen for obtaining the high-resolution optical spectrum of ζ Aurigae and N. Piskunov for his reduction and analysis of these data. C. A. H. thanks his colleagues and especially Lu Rarogiewicz and Craig Denison for their help with the Mark III observations. The authors are also grateful to Daniel Schaerer for making the stellar models of Schaller et al. (1992) and Schaerer et al. (1993) available via anonymous ftp.

APPENDIX

In this appendix we describe the use of the C I interstellar lines as a standard wavelength reference to calibrate the GHRS G160M spectra. We report on this wavelength calibration procedure in considerable detail because the results of our analysis depend critically on its reliability.

TABLE 12

THE C I UV 5, 6, AND 7 MULTIPLETS

λ_{lu} (Å)	Multiplet	Term	J_l	J_u	g_l	E_l (cm^{-1})	f_{lu}
1277.245......	UV 7	^3P–$^3D^o$	0	1	1	0.00	8.91(−2)
1277.282......	UV 7	^3P–$^3D^o$	1	2	3	16.40	6.80(−2)
1277.513......	UV 7	^3P–$^3D^o$	1	1	3	16.40	2.25(−2)
1279.056......	UV 6	^3P–$^3F^o$	1	2	3	16.40	1.60(−3)
1279.890......	UV 5	^3P–$^3P^o$	1	2	3	16.40	2.06(−2)
1280.135......	UV 5	^3P–$^3P^o$	0	1	1	0.00	4.90(−2)
1280.404......	UV 5	^3P–$^3P^o$	1	1	3	16.40	1.24(−2)
1280.597......	UV 5	^3P–$^3P^o$	1	0	3	16.40	1.63(−2)

Ultraviolet multiplets 5, 6, and 7 of C I have lines between 1277 and 1281 Å. These lines are listed in Table 12, with laboratory wavelengths from Kelly & Palumbo (1973) and oscillator strengths from the Kurucz (1990) line list. Only two of these lines are seen in the observed spectrum of ζ Aur: a line near 1277.3 Å (λ1277) and another at 1280.2 Å (λ1280). Figure 15 shows the observed spectrum in the region of these C I lines at Epoch 1. Evidently, λ1280 is the C I UV 5$^3P_0$–$^3P_1^o$ line at 1280.135 Å, while λ1277 is a blend of the C I UV 7 $^3P_0$–$^3D_1^o$ and $^3P_1$–$^3D_2^o$ lines. In order to use λ1277 as a radial velocity reference, we need an estimate of the effective laboratory wavelength of the blend. The following analysis requires two assumptions: (1) the C I lines are optically thin, which is reasonable since the residual intensity in the lines is greater than 0.6, and (2) the line profiles are Gaussian. The first assumption allows relative populations of the fine-structure levels of the C I ground state to be inferred directly from analysis of the equivalent widths, and the second assumption allows the centroid of blended lines to be calculated.

The populations of the C I ground state fine-structure levels ($J = 0$, 1) contributing to λ1277 are determined by a similar analysis of the C I UV 3 resonance multiplet near 1560 Å. The UV 3 transitions, wavelengths, and oscillator strengths are taken from the same sources as the UV 5, 6, and 7 multiplets. The data for the C I UV 3 multiplet are listed in Table 13. In the 1560 Å region, two well-separated lines originating from the $J = 0$ and $J = 1$ fine-structure levels are observed. The first of these lines, observed at 1560.36 Å (λ1560), is the C I UV 3 $^3P_0$–$^3D_1^o$ line at 1560.3095 Å. The second feature, λ1561, is a blend of the $^3P_1$–$^3D_2^o$ and $^3P_1$–$^3D_1^o$ lines. Both lines come from the $J = 1$ level, and so the blend can still be used for inferring the $J = 1$ level population. The mean equivalent widths observed for these lines (averaged over epochs 3 and 6) are $W_{1560} = 53.4$ mÅ

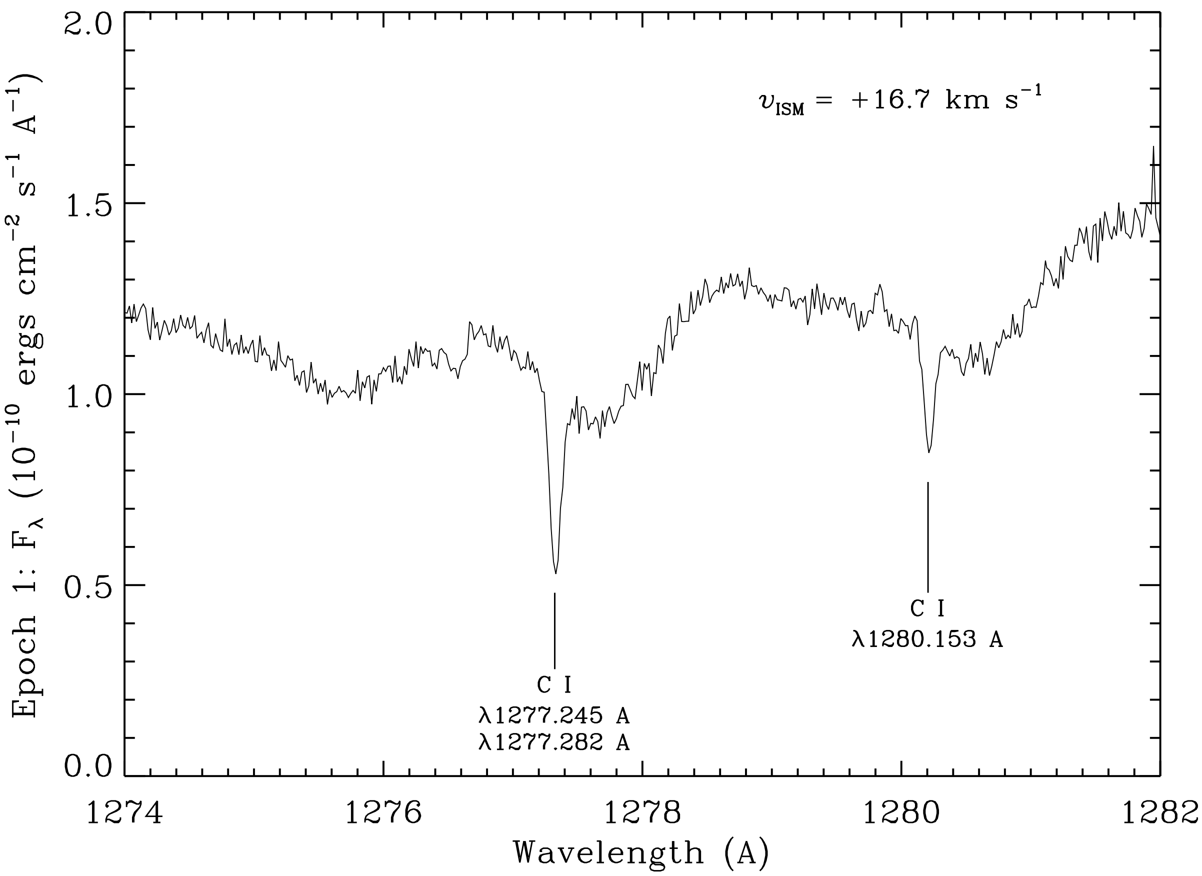

FIG. 15.—Region of the spectrum of ζ Aurigae observed at Epoch 1 with the G160M medium-resolution grating of the GHRS. The two prominent sharp lines are due to interstellar C I and are used to provide an absolute wavelength reference for the radial velocity analysis.

TABLE 13

THE C I ^3P–$^3D^o$ UV 3 MULTIPLET

λ_{lu} (Å)	J_l	J_u	g_l	E_l (cm^{-1})	f_{lu}
1560.3095......	0	1	1	0.00	7.58(−2)
1560.6832......	1	2	3	16.40	5.66(−2)
1560.7079......	1	1	3	16.40	1.92(−2)
1561.3407......	2	2	5	43.40	1.15(−2)
1561.367	2	1	5	43.40	7.60(−4)
1561.4382......	2	3	5	43.40	6.32(−2)

TABLE 14

OBSERVED VELOCITIES OF C I UV 3 INTERSTELLAR LINES

Epoch	λ1277 (Å)	$V_{\rm ISM}$	λ1280 (Å)	$V_{\rm ISM}$	$\langle V_{\rm ISM}\rangle$
1......	1277.3210	+16.20	1280.2084	+17.19	+16.70
2......	1277.3084	+13.24	1280.1937	+13.75	+13.50
3......	1277.3249	+17.11	1280.2113	+17.87	+17.49
6......	1277.3085	+13.26	1280.1911	+13.14	+13.20

and $W_{1561} = 17.2$ mÅ. We find the relative level populations ε_J of the Jth C I fine-structure levels to be $\varepsilon_0 = 0.765$ and $\varepsilon_1 = 0.244$, where $\sum_i \varepsilon_i = 1$.

The centroid of a blend of two absorption lines (assuming Gaussian profiles), at wavelengths λ_a, λ_b and with equivalent widths W_a, W_b, respectively, is given by

$$\lambda_{ab} = \lambda_a\left(\frac{1}{1+r}\right) + \lambda_b\left(\frac{r}{1+r}\right) , \tag{A1}$$

where $r = W_b/W_a$. Using the populations ε_0, ε_1 of the C I fine-structure levels determined from λ1560 and λ1561, we can evaluate the ratio of equivalent widths of the lines contributing to the λ1277 blend. We obtain

$$r = \frac{W_{12}}{W_{01}} = \frac{\varepsilon_1 f_{12}}{\varepsilon_0 f_{01}} = 0.246 , \tag{A2}$$

where the subscripts ij refer to the transitions ^3P_i–$^3D^o_j$. Therefore, the effective rest wavelength of the λ1277 blend is

$$\lambda 1277 = 0.803\lambda_{01} + 0.197\lambda_{12} = 1277.252 \text{ Å} . \tag{A3}$$

This wavelength is used for determining radial velocities of the λ1277 blend. The radial velocities of the observed λ1277 and λ1280 lines, calculated assuming rest wavelengths of 1277.252 Å and 1280.135 Å, respectively, are tabulated in Table 14. The mean of the ISM radial velocity values obtained from λ1277 and λ1280 for each of the epochs 1,2,3, and 6 appears in Table 14 as $\langle V_{\rm ISM}\rangle$. The actual velocity of the interstellar medium, $V_{\rm ISM}$, is related to the value of $\langle V_{\rm ISM}\rangle$ found at epoch i ($\langle V_{\rm ISM}\rangle_i$) by $V_{\rm ISM} = \langle V_{\rm ISM}\rangle_i + V^0_i$, where V^0_i is the (unknown) zero-point error in the GHRS wavelength calibration. Since $V_{\rm ISM}$ will not vary with observation epoch, we difference the expression for $V_{\rm ISM}$ at epochs i and j to obtain the differential zero-point error,

$$\Delta V^0_{ij} = V^0_i - V^0_j = \langle V_{\rm ISM}\rangle_j - \langle V_{\rm ISM}\rangle_i . \tag{A4}$$

The ΔV^0_{ij} values are tabulated in the fifth column of Table 4 and are seen to be consistent with the 3.5 km s^{-1} precision expected from the wavelength-calibrated G160M spectra.

REFERENCES

Allen, C. W. 1976, Astrophysical Quantities (3d ed.; London: Athlone)
Alongi, M., Bertelli, G., Bressan, A., Chiosi, C., Fagotto, F., Greggio, L., & Nasi, E. 1993, A&AS, 97, 851
Anders, E., & Grevesse, N. 1989, Geochim. Cosmochim. Acta, 53, 197
Armstrong, J. T., et al. 1992, AJ, 104, 241
Batten, A. H., Fletcher, J. M., & MacCarthy, D. G. 1989, Publ. Dom. Astrophys. Obs., 17, 1
Bennett, P. D., Brown, A., & Linsky, J. L. 1995, ApJ, 455, 317 (Paper I)
Bertelli, G., Bressan, A., Chiosi, C., Fagotto, F., & Nasi, E. 1994, A&AS, 106, 275
Bressan, A., Fagotto, F., Bertelli, G., & Chiosi, C. 1993, A&AS, 100, 647
Brown, A., Bennett, P. D., Harper, G. M., Linsky, J. L., Baade, R., Kirsch, T., & Reimers, D. 1996, in preparation
Campbell, B., Walker, G. A. H., & Yang, S. 1988, ApJ, 331, 902
Cardelli, J. A., Clayton, G. C., & Mathis, J. S. 1989, ApJ, 345, 245 (CCM)
Chuma, J. L., Bennett, P. D., & Kost, C. J. 1996, in preparation
Di Benedetto, G. P., & Ferluga, S. 1990, A&A, 236, 449
Eaton, J. A. 1993, ApJ, 404, 305
Erhorn, G. 1990, Ph.D. thesis, Univ. of Hamburg
Grant, G., & Abt, H. A. 1959, ApJ, 129, 320
Green, R. M. 1985, Spherical Astronomy (Cambridge: Cambridge Univ. Press)
Griffin, R. E. M., Griffin, R. F., Schröder, K.-P., & Reimers, D. 1990, A&A, 234, 284
Griffin, R. F. 1995, private communication
Hanbury Brown, R., Davis, J., Lake, R. J. W., & Thompson, R. J. 1974, MNRAS, 167, 475
Harper, G. M., Bennett, P. D., & Brown, A. 1996, in preparation
Harper, W. E. 1924, Publ. Dom. Astrophys. Obs., 3, 151
Hubeny, I. 1988, Comput. Phys. Comm., 52, 103
Hummel, C. A., & Armstrong, J. T. 1994, in Very High Angular Resolution Imaging, ed. J. G. Robertson & W. J. Tango (Dordrecht: Kluwer), 410
Hummel, C. A., Armstrong, J. T., Quirrenbach, A., Buscher, D. F., Mozurkewich, D., Simon, R. S., & Johnston, K. J. 1993, AJ, 106, 2486
Iglesias, C. A., Rogers, F. J., & Wilson, B. G. 1992, ApJ, 397, 717
Johnson, H. L. 1965, ApJ, 141, 923
Kelly, R. L., & Palumbo, L. J. 1973, Atomic and Ionic Emission Lines Below 2000 Angstroms, NRL Report 7599 (Washington: Naval Research Laboratory)
Kiyokawa, M. 1967, PASJ, 19, 209

Koppmann, R. 1985, Ap&SS, 110, 321
Kurucz, R. L. 1990, Trans. IAU, 20B, 169
Lee, E. K., & Wright, K. O. 1960, Publ. Dom. Astrophys. Obs., 11, 339
Lovell, L. P., & Hall, D. S. 1973, PASP, 85, 131
McWilliam, A. 1990, ApJS, 74, 1075
Mozurkewich, D., et al. 1991, AJ, 101, 2207
Piskunov, N. P. 1995, private communication
Popper, D. M. 1961, ApJ, 134, 828
Rieke, G. H., & Lebofsky, M. J. 1985, ApJ, 288, 618
Rogers, F. J., & Iglesias, C. A. 1992, ApJS, 79, 507
Sanwal, N. B., Parthasarathy, M., & Abhyankar, K. D. 1973, Observatory, 93, 30
Schaerer, D., Meynet, G., Maeder, A., & Schaller, G. 1993, A&AS, 98, 523
Schaller, G., Schaerer, D., Meynet, G., & Maeder, A. 1992, A&AS, 96, 269
Shao, C.-Y. 1964, AJ, 69, 858
Shao, M., et al. 1988, A&A, 193, 357
Soderblom, D. R., Hulbert, S. J., Leitherer, C., & Sherbert, L. E. 1994, Instrument Handbook for the Goddard High Resolution Spectrograph (GHRS), vers. 5.0 (Baltimore: STScI)
van Genderen, A. M. 1964, Bull. Astron. Inst. Netherlands, 17, 446
Van Hamme, W. 1993, AJ, 106, 2096
Wood, F. B. 1951, AJ, 56, 53
Wood, F. B., Oliver, J. P., Florkowski, D. R., & Koch, R. H. 1980, A Finding List for Observers of Interacting Binaries (Philadelphia: Univ. of Pennsylvania Press)
Wright, K. O. 1970, Vistas Astron., 12, 148